Characterization of potential nanoporous sodium titanate film formation on Ti6Al4V and TiO$_2$ microspherical substrates *via* wet-chemical alkaline conversion

Matthew D. Wadge [a,*], Matthew J. Carrington [a], Hannah Constantin [a], Kieran Orange [a], Jason Greaves [a], Md Towhidul Islam [a,b], Kazi M. Zakir Hossain [c], Timothy P. Cooper [d], Zakhar R. Kudrynskyi [a], Reda M. Felfel [a,e], Ifty Ahmed [a], David M. Grant [a,*]

[a] *Advanced Materials Research Group, Faculty of Engineering, University of Nottingham, UK*
[b] *Department of Applied Chemistry and Chemical Engineering, Faculty of Engineering, Noakhali Science and Technology University, Noakhali 3814, Bangladesh*
[c] *Department of Chemistry, University of Bath, Claverton Down, Bath, UK*
[d] *Advanced Manufacturing Technology Research Group, Faculty of Engineering, University of Nottingham, UK*
[e] *Physics Department, Faculty of Science, Mansoura University, Mansoura, Egypt*

ARTICLE INFO

ABSTRACT

The authors present novel insights into the formation of nanoporous, wet-chemically produced sodium titanate films onto microspherical substrates of varying composition. Microspheres of Ti6Al4V (atomised; *ca.* 20–50 μm), which were utilised due to their ubiquitous industrial usage relative to metallic titanium, were compared with TiO$_2$ microspheres (flame spheroidised anatase and rutile powders; average *ca.* 30–40 μm). These were then suspended in 5 M NaOH solutions (60 °C, 24 h), and then characterized (SEM, EDS, XRD, XPS) to determine the extent of sodium titanate generation, and the potential inhibition of formation due to oxygen content. It was found that excessive oxygen content (flame-spheroidised rutile and anatase powders) resulted in inhibition of nanoporous titanate formation, apart from the top few nanometres of the surface, since a diffusion barrier of TiO$_2$ prevents further conversion. The characteristic nanoporous titanate structures were formed on the Ti6Al4V microspheres, *ca.* 1 μm (999 ± 25 nm) in thickness, whereas no visible alteration to the TiO$_2$ microspheres were seen. High surface concentration (*ca.* 9.5–17.6 at.%) of Na was seen in all samples *via* XPS, including the TiO$_2$ microspheres (despite no morphological change), however, only the Ti6Al4V microspheres exhibited moderate Na content (*ca.* 4.7 at.%) *via* EDS, illustrating a diffusion gradient during formation. The confirmation of these structures onto microspherical substrates opens the possibility for application in biomaterials, water treatment, and energy fields.

1. Introduction

Alkaline titanate structures have garnered significant attention, in a wide variety of fields, due to their multifunctional properties [1,2]. Fields such as photocatalysis [3], biomaterials [4], radioactive waste-water treatment [5], and batteries [6], just to name a few, have benefited from the research into these structures. Their ability to translate so easily between fields is due to their ion-exchangeability [7–9], functionalisation [10], simplistic methodology [11], as well as their production into a number of different morphologies; from 1D nanostructures [12], to 2D exfoliated nanosheets and 3D nanotubes

[13], as well as formation onto varying alloy compositions; from Ti—Nb [14], to Gummetal® (Ti$_{59}$Nb$_{36}$Ta$_2$Zr$_3$O$_{0.3}$) [15], to the widely used Ti6Al4V [16]. Specifically in a biomedical context, the ability to dope such structures with specific ions can result in either bioactive and/or antimicrobial properties, which address significant problems currently with implant failure rates and the ever-increasing severity of antibiotic resistance [17–19].

The present authors have conducted several published studies looking into the formation of nanoporous alkaline titanate films, as opposed to nano-tubular and nano-sheet formations, mainly for biomedical applications. This is due to the improved cellular viability on

such nanoporous structures, with enhanced functionality *via* cationic exchange. From work into antibacterial gallium-doping of the sodium hydrogen titanate structure (one of the first studies to investigate gallium-doping of such structures) [20], to the potential translation of nanoporous sodium titanate coatings onto the surface of alternative, non-Ti containing materials (316 L SS [21], Mg [22]) through conversion of sputtered Ti films, information has been gleaned regarding the formation mechanism of these structures. Since the seminal work by Kim et al. [23] and Kokubo et al. [24], a great deal of work has been conducted into various aspects of alkaline titanate formation. These include: the formation of nanotubes as carrier material for cellular stimuli applications (drug delivery, protein carriers, *etc.*) onto Ti and TiO_2 substrates using various temperatures and concentrations [25–29] compared to the widely used 5 M, 60 °C, 24 h NaOH solution treatment that produces nanoporous films; nanowhiskers and nanowire scaffolds have be used to encourage proliferation of MG63 osteoblast cells [30]; as well as formation of titanate spheres, with enhanced porosities of up to 200 µm [31]. However, the production of nanoporous titanate films onto microspherical substrates is somewhat limited in the literature, as well as comparing this with TiO_2 microspheres.

The present authors aim to elucidate the effect of microspherical nature of the substrates, and their relative oxygen content, on the initial formation of nanoporous titanate films utilising lower temperature/concentration conditions (5 M NaOH; 60 °C; 24 h), and whether this agrees with common consensus on the titanate formation mechanism, as outlined by Kim et al. [23] and Kokubo [32]. Initially, the TiO_2 passivated layer on the surface is partially dissolved due to corrosive attack of hydroxyl groups.

$$TiO_2 + OH^- \rightarrow HTiO_3^- \tag{1}$$

Simultaneously, hydration of the underlying Ti metal due to diffusion processes occurs, enabling the foundation for subsequent titanate formation:
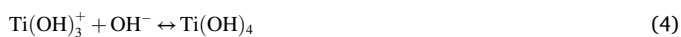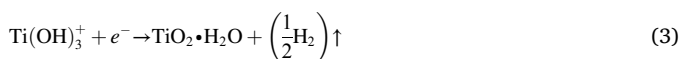
$$Ti + 3OH^- \rightarrow Ti(OH)_3^+ + 4e^- \tag{2}$$

$$Ti(OH)_3^+ + e^- \rightarrow TiO_2 \cdot H_2O + \left(\frac{1}{2}H_2\right)\uparrow \tag{3}$$

$$Ti(OH)_3^+ + OH^- \leftrightarrow Ti(OH)_4 \tag{4}$$

Consequently, the hydrated TiO_2 formed from the aforementioned reactions generates negatively charged titanium oxide hydrates.

$$TiO_2 \cdot nH_2O + OH^- \leftrightarrow HTiO_3^- \cdot nH_2O \tag{5}$$

Since these structures are negatively charged, combination with alkali ions in solution occurs, which in the case of NaOH is Na^+ to form sodium (hydrogen) titanate structures. By altering the morphology and composition of the initial substrate, despite both possessing a top surface of TiO_2, the authors postulated that either the limitation of free Ti within the structure reduces the ability to form such structures, the increased oxygen content enables greater penetration and formation into thicker and/or denser titanate films, the microspherical nature of the substrate may have higher reactivity due to increased surface area, and/or TiO_2 would provide higher stability in NaOH solutions compared to pure Ti. These postulates were investigated in this study.

In addition, limited research had been conducted on the wet-chemical production of alkaline titanate layers on Ti-containing microspheres [33]. Therefore, this study investigated the effect of oxygen (O) content in Ti based microspheres, comparing Ti6Al4V and TiO_2 microspheres due to the relative ease of producing Ti6Al4V and TiO_2 microspheres of similar size and the industrial importance in the biomedical and energy fields, to ascertain whether titanate structures could be produced on 3D surfaces, using the same wet chemical conditions.

2. Materials and methods

2.1. Powders

Plasma atomised Ti6Al4V Grade 23 powder (LPW Technologies, UK; Fig. 1A) was utilised as the base material for the self-assembly study. The powder was provided by Dr. Nesma T. Aboulkhair (Additive Manufacturing and 3D Printing Research Group, University of Nottingham), with the D_{10}, D_{50}, and D_{90} values, calculated *via* a Mastersizer 3000 (Malvern, UK) laser diffraction method, of 19.6, 31.5 and 49.1 µm, respectively [34]. Ti6Al4V microspheres are herein labelled: Ti6Al4V_MS.

The TiO_2 microspheres were produced in house (Advanced Materials Research Group, University of Nottingham) through flame-spheroidisation (FS) of anatase and rutile powders. Granular particles (<150 µm; ImageJ analysis demonstrated average particle sizes of 37.5 ± 0.7 and 35.8 ± 0.9 µm for anatase and rutile particles, respectively) were prepared by mixing TiO_2 (<5 µm; ≥99%, Sigma Aldrich, UK; Both anatase and rutile powder used separately) and 2% polyvinyl alcohol (PVA; ≥99%, Sigma Aldrich, UK) solution. The mixture was then processed utilising a flame spheroidisation process to prepare solid microspheres, which utilised an oxy/acetylene flame spray gun (MK 74, Metallisation Ltd., UK) (Fig. 1B & C) [35]. TiO_2 microspheres produced using anatase powder are herein labelled: FS_Anatase_MS. TiO_2 microspheres produced using rutile powder are herein labelled: FS_Rutile_MS.

2.2. Wet-chemical conversion

The Ti6Al4V and TiO_2 microspheres were suspended in a *ca.* 5 M NaOH solution prepared using NaOH pellets (*ca.* 19.99 g per 100 mL of distilled water; 99.9% purity; Sigma-Aldrich). 10 mL aliquots of the NaOH solution were dispensed into polypropylene containers, which contained 5 g of either of the studied microspheres. These were then sealed and heated in a low temperature furnace at 60 ± 2 °C for 24 h. Upon removal, the microspheres were washed *via* filtration in deionised water to remove excess NaOH, before furnace drying at 100 °C for 1 h (in air), followed by storage within a desiccator until testing. These samples are herein labelled with the suffix: NaTC.

2.3. Characterization

2.3.1. Scanning electron microscopy (SEM) & energy dispersive X-ray spectroscopy (EDS)

Image acquisitions for higher resolution micrographs were conducted on a Field-Emission Gun Scanning Electron Microscope (JEOL 7100 FEG-SEM). Surface compositional analysis was determined *via* an Energy-Dispersive X-ray spectrometer (EDS) (Oxford Instruments) at a working distance of 10 mm, a beam voltage of 15 kV, whilst maintaining a minimum X-ray count of 150,000 counts.

2.3.2. X-ray photoelectron spectroscopy (XPS)

All samples were mounted onto stainless steel stubs using carbon sticky tabs. X-ray Photoelectron Spectroscopy (XPS) was conducted using a VG ESCALab Mark II X-ray photoelectron spectrometer with a monochromatic Al Kα X-ray source incident to the sample surface at ≈30°. Survey and high-resolution scans were conducted in addition to the measurement of adventitious C 1s for calibration: charge corrected to 284.8 eV. Parameters for acquisition were as follows: step size of 1.0; number of scans set at 5; dwell time 0.2 s for survey scans, and 0.4 s for high-resolution scans. Binding energies were measured over a range of 0–1200 eV. All spectra were analysed in CasaXPS constraining the Full Width at Half Maximum (FWHM) to the same value for all deconvoluted spectral peaks for the same element.

2.3.3. X-ray diffraction (XRD)

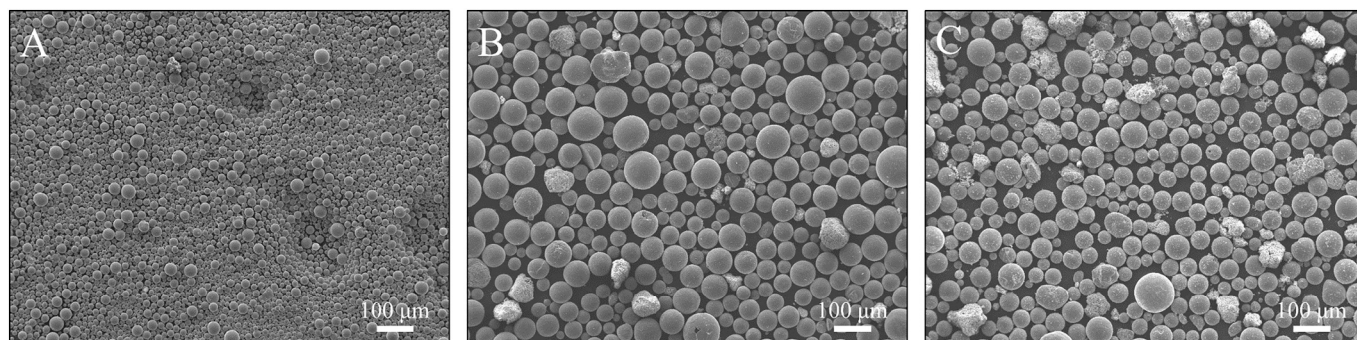X-ray diffractograms of the pre- and post-titanate converted samples

Fig. 1. Micrographs of microspheres utilised within this study. A) Ti6Al4V microspheres produced *via* atomisation; B) TiO$_2$ microspheres produced from anatase powder *via* flame spheroidisation; C) TiO$_2$ microspheres produced from rutile powder *via* flame spheroidisation.

were recorded using a Bragg-Brentano configured Bruker D8 employing Cu K-α radiation, which was operated at a working voltage and current of 40 kV and 40 mA, respectively. This machine is equipped with a LYNXEYE XE-T position sensitive (1D) energy discriminating detector, a variable anti-scatter screen, variable divergent slits, and a variable detector window. Measurements were taken with a step size of 0.02° between 20 and 100° 2θ. Rietveld refinements [36] were performed using Topas V6 software and the fundamental parameters approach to X-ray line profile fitting was employed [37,38].

2.3.4. Raman spectroscopy

Raman spectroscopy was achieved utilising a HORIBA Jobin Yvon LabRAM HR spectrometer. Spectra were acquired using a 660 nm laser (100 mW power), 100× objective, 300 μm confocal pinhole and a 600 lines/mm rotatable diffraction grating along a path length of 800 mm. Detection of spectra was attained through the use of a thermoelectrically cooled (−60 °C) SYNAPSE CCD detector (1024 pixels). Instrument calibration was conducted using a standard Si (100) reference (standard band at 520.7 cm^{-1}) and the Rayleigh line at 0 cm^{-1}, prior to spectra acquisition. A constrained time window of 10 s was employed for each spectrum recording with 10 accumulations.

2.3.5. Mercury porosimetry

The porosity of the microsphere surfaces was investigated using mercury intrusion porosimetry (Micromeritics Autopore IV 9500). A 5 cc powder penetrometer (Micrometrics) with 1 cc intrusion volume was used for all samples. An empty penetrometer test was also conducted as

a blank before running the samples.

3. Results

3.1. SEM/EDS

As observed in Fig. 2A-C, the Ti6Al4V microspheres (Ti6Al4V_MS) exhibited a relatively smooth morphology produced *via* the atomisation process. However, following wet-chemical conversion in NaOH (Ti6Al4V_MS NaTC), a nanoporous morphology characteristic of titanate structures was present, with clear morphological differences (Fig. 2C & F) noted between pre- (_MS) and post-titanate (_MS NaTC) converted samples. In some cases, cross growth and bonding between titanate structures of neighbouring microspheres was exhibited, with examples of bonded (Fig. 3A & B) and fractured structures (Fig. 3C & D); fracturing occurred due to removal of the spheres from their container.

Delamination of the fracture structures occurred predominantly at the interface of the Ti substrate, and the titanate formed layer, which is clearly exhibited in Fig. 3C & D, as both fracture ends revealed a smooth morphology, matching the underlying microsphere surface texture. Thickness of the titanate structures were analysed using SEM and ImageJ analysis, with the main thickness defined (detailed in Fig. 4) as the average height of the individual titanate dendrite extensions. This thickness was found to be 999 ± 25 nm (*n* = 10).

When the same chemical conversion was applied to titania (TiO$_2$) microspheres, the morphology of the microspheres (size range *ca.* 10–100 μm) did not produce any discernible change in structure of the
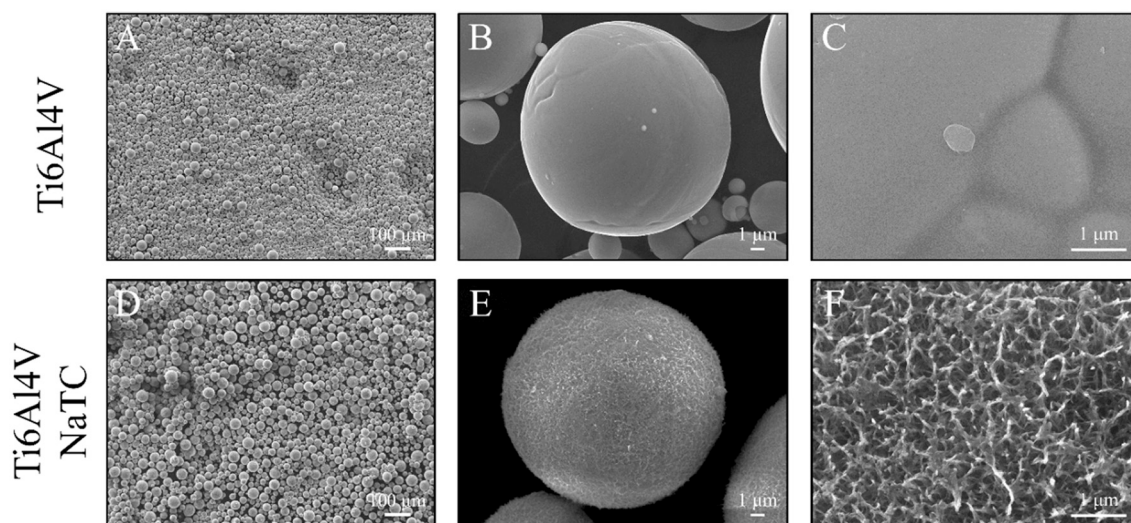

Fig. 2. SEM micrographs showing unconverted (Ti6Al4V_MS) and converted (Ti6Al4V_MS NaTC) Ti6Al4V microspheres demonstrating the ability to convert the surface into nanoporous titanate structures. A, B & C) Unconverted Ti6Al4V_MS samples, and D, E & F) Converted Ti6Al4V_MS NaTC samples.
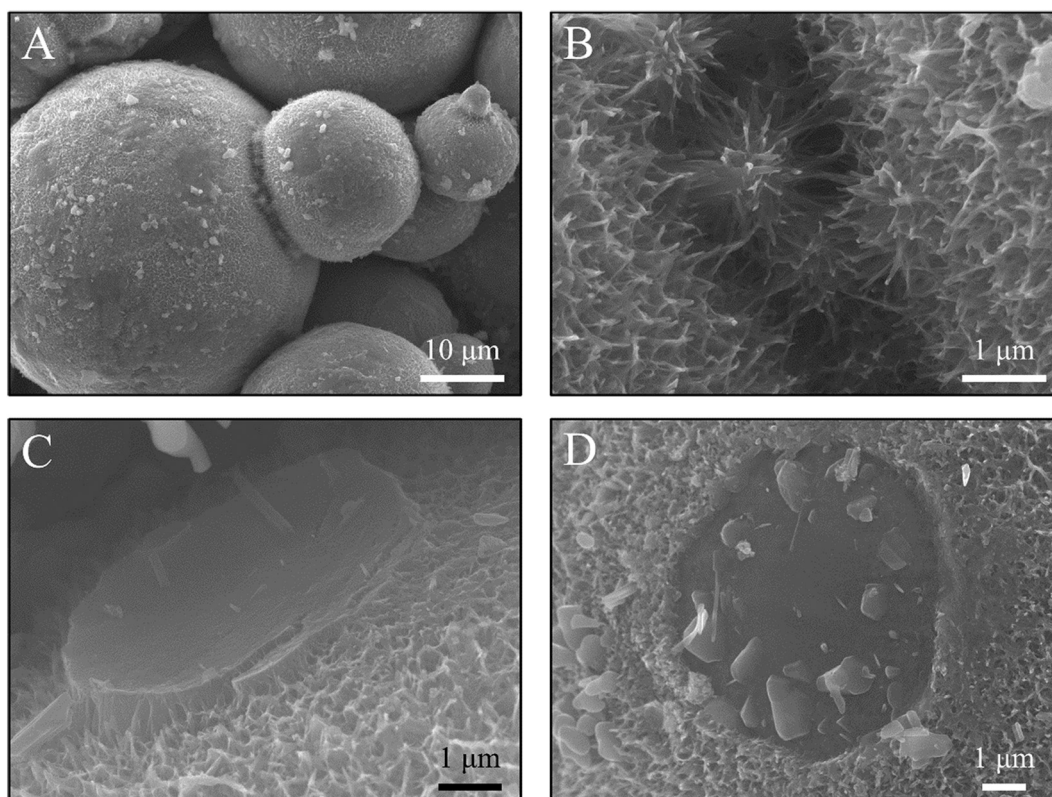
Fig. 3. SEM micrographs showing cross growth and fracture features noted on the titanate converted Ti6Al4V microspheres (Ti6Al4V_MS NaTC). A) & B) Cross-linking of two individual microspheres through the growth and bonding of the produced titanate nanostructures at different magnifications. C) & D) Smooth morphology of the microsphere surfaces at the failure of the bonded interface at either end of the failure.
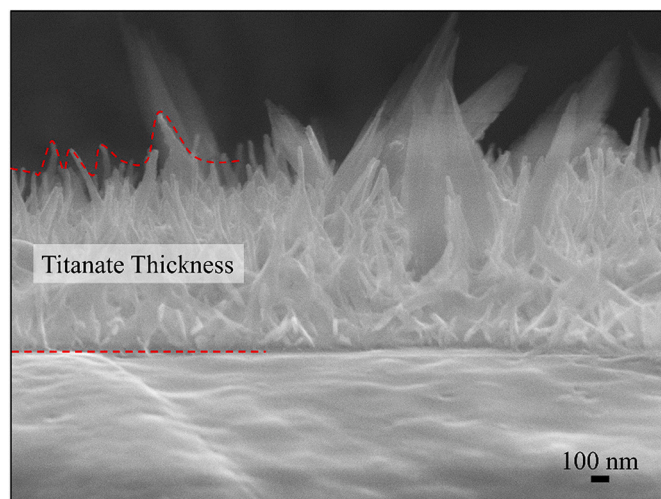

Fig. 4. SEM micrograph demonstrating a representative thickness of the titanate constructs on the Ti6Al4V microspheres (Ti6Al4V_MS NaTC). The main thickness was defined as the average height of the individual extended titanate dendrites ($n = 10$).

produced microspheres, aside from removal of surface particulates (Fig. 5). However, small levels of Na were seen on the surface from EDS analysis (Table 1); it was hypothesised that the level of oxygen content in the surface had a marked influence of the growth mechanism seen. In comparison to the Ti6Al4V_MS NaTC samples, the Na levels were significantly lower for the FS_Anatase_MS NaTC and FS_Rutile_MS NaTC samples, with *ca.* 4.7, 0.5 and 0.2 at.%, for the Ti6Al4V_MS NaTC, FS_Anatase_MS NaTC, and FS_Rutile_MS NaTC samples, respectively; the

latter two results are below the threshold for accurate assessment *via* EDS (*ca.* 1 at.%). A significant reduction in Ti (*ca.* 87 to 31 at.%) and increase in O (*ca.* 0 to 61 at.%) content was noted for the Ti6Al4V_MS, compared to the Ti6Al4V_MS NaTC samples. Both the anatase and rutile samples maintained constant Ti (*ca.* 30–32 at.%) and O (*ca.* 68–70 at.%) levels.

The EDS mapping presented in Fig. 6 shows that Ti, O and Na (present in the NaTC samples only) were homogeneously distributed across the spheres. Higher relative quantities of Na (in relation to Ti and O) in the Ti6Al4V_MS NaTC sample were observed compared to both the FS_Anatase_MS NaTC and FS_Rutile_MS NaTC samples (Table 1).

3.2. XPS analysis

XPS analysis of both the titanate converted and non-titanate converted Ti6Al4V and TiO_2 (flame-spheroidised anatase and rutile) microspheres are detailed in Fig. 7, Table 2 & Table 3. For the Ti6Al4V_MS samples, the Ti was found to be in its 4^+ valence state (2p 3/2 = *ca.* 458.7 eV), characteristic of the passivated TiO_2 layer that forms due to exposure to air. O had 2 peak deconvolutions located at *ca.* 530.3 (60.5%) and 532.3 (39.5%) eV corresponding to metallic oxide and hydroxide bonding, respectively. Upon conversion to sodium titanate (Ti6Al4V_MS NaTC), there was a shift (*ca.* 0.7 eV) to lower binding energies in the Ti peak position (*ca.* 458.0 eV), which was characteristic of Ti^{4+} within titanate structures. There was an increase in the number of O peak deconvolutions, with 4 peaks located at *ca.* 529.6, 531.3, 532.5 and 534.9 eV corresponding to O^{2-} (*ca.* 54.7%; Ti^{4+}—O), bridging OH^-_{br}/defective oxides/Non-lattice O (*ca.* 24.0%), terminal OH^-_t/H_2O (*ca.* 9.4%), and Na KLL Auger e^- (*ca.* 11.8%), respectively. A peak was also formed at 1071.1 eV corresponding the Na—O bonding of titanate structures, with two Ti LMM Auger peaks that were also present in the Ti6Al4V_MS sample.
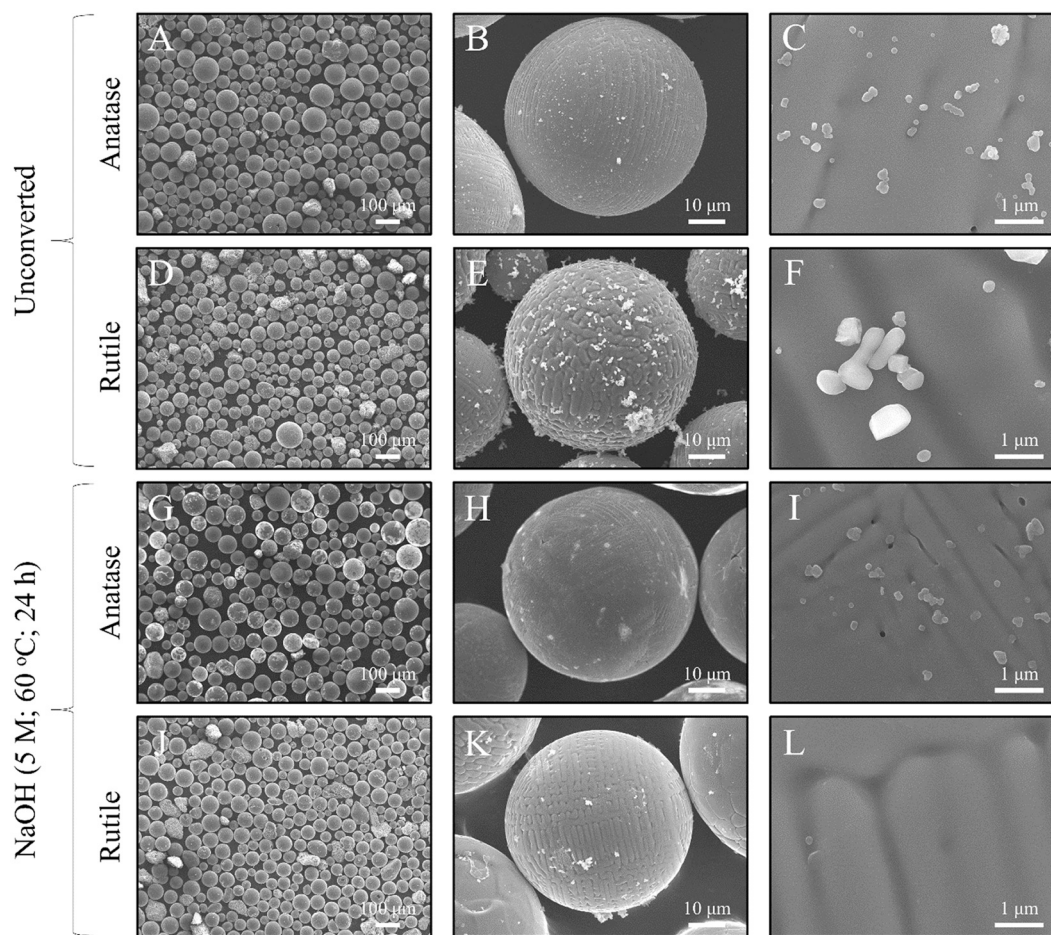
Fig. 5. TiO$_2$ microspheres produced *via* a flame spheroidisation process using rutile or anatase starting powder, with subsequent titanate (NaTC) conversion. A–C) FS_Anatase_MS; D–F) FS_Rutile_MS; G–I) FS_Anatase_MS NaTC; J–L) FS_Rutile_MS NaTC.

Table 1
EDS elemental composition of Ti6Al4V, Anatase and Rutile microspheres (Ti6Al4V_MS, FS_Anatase_MS, and FS_Rutile_MS, respectively), as well as sodium titanate conversion of all three types, herein labelled with NaTC suffix. All values are mean ± standard error (*n* = 3).

Sample ID	Elemental composition / at.%				
	Na	Ti	O	Al	V
Ti6Al4V_MS	0	86.7 ± 0.1	0	9.4 ± 0.1	3.9 ± 0.1
Ti6Al4V_MS NaTC	4.7 ± 0.3	30.9 ± 0.7	60.5 ± 0.5	2.6 ± 0.1	1.4 ± 0.1
FS_Anatase_MS	0	30.0 ± 3.6	70.0 ± 3.6	0	0
FS_Anatase_MS NaTC	0.5 ± 0.1	31.0 ± 1.9	68.4 ± 1.9	0	0
FS_Rutile_MS	0	31.3 ± 3.3	68.7 ± 3.3	0	0
FS_Rutile_MS NaTC	0.2 ± 0.0	30.0 ± 3.3	69.8 ± 3.2	0	0

For the FS_Anatase_MS and FS_Rutile_MS samples, similar peak deconvolutions to the Ti6Al4V_MS sample were noted. Ti was found in its 4$^+$ valence state (*ca.* 458.4–458.6 eV), and the O deconvolutions revealed two peaks at *ca.* 529.9 (73.6–78.2%) and 532.2 (21.8–26.4%) eV, again corresponding to the aforementioned bonding. Following titanate conversion, both the FS_Anatase_MS NaTC and FS_Rutile_MS NaTC samples again exhibited similar deconvolutions to the Ti6Al4V_MS NaTC counterpart, with notable shifts in binding energies for both Ti and O to lower eV values. The peak deconvolutions for the O spectral range exhibited 4 peaks located at *ca.* 529.4 (*ca.* 28.1%), 531.2 (*ca.* 38.3%), 532.8 (*ca.* 17.1%), and 535.5 (*ca.* 16.5%) eV for the FS_Anatase_MS NaTC samples, whilst the FS_Rutile_MS NaTC sample exhibited peaks at *ca.* 529.6 (*ca.* 16.8%), 531.6 (*ca.* 31.2%), 533.0 (*ca.* 45.0%), and 535.6 (*ca.* 7.0%) eV, corresponding to O^{2-} (Ti^{4+}—O), bridging OH$^-_{br}$/defective oxides, terminal OH^-_t/H$_2$O, and Na KLL

Auger *e*$^-$, respectively. The relative percentages of each type of bonding, specifically the reduction in Ti^{4+}—O bonding characteristic of titanate structures, demonstrated that the quantity of surface titanate that formed was considerably less for the FS_Anatase_MS NaTC and FS_Rutile_MS NaTC, and may only be present in the top few nanometres of the surface.

It was clear from the relative elemental compositions (Table 3) that the Ti6Al4V_MS NaTC samples exhibited higher Na content compared to both converted anatase and rutile samples, however, there was no significant difference between the FS_Anatase_MS NaTC and Ti6Al4V_MS NaTC samples. Furthermore, the Ti and O content for the Ti6Al4V_MS and Ti6Al4V_MS NaTC samples remained constant, however, the anatase and rutile counterparts exhibited a reduction in Ti (O content increased for rutile but decreased for anatase).
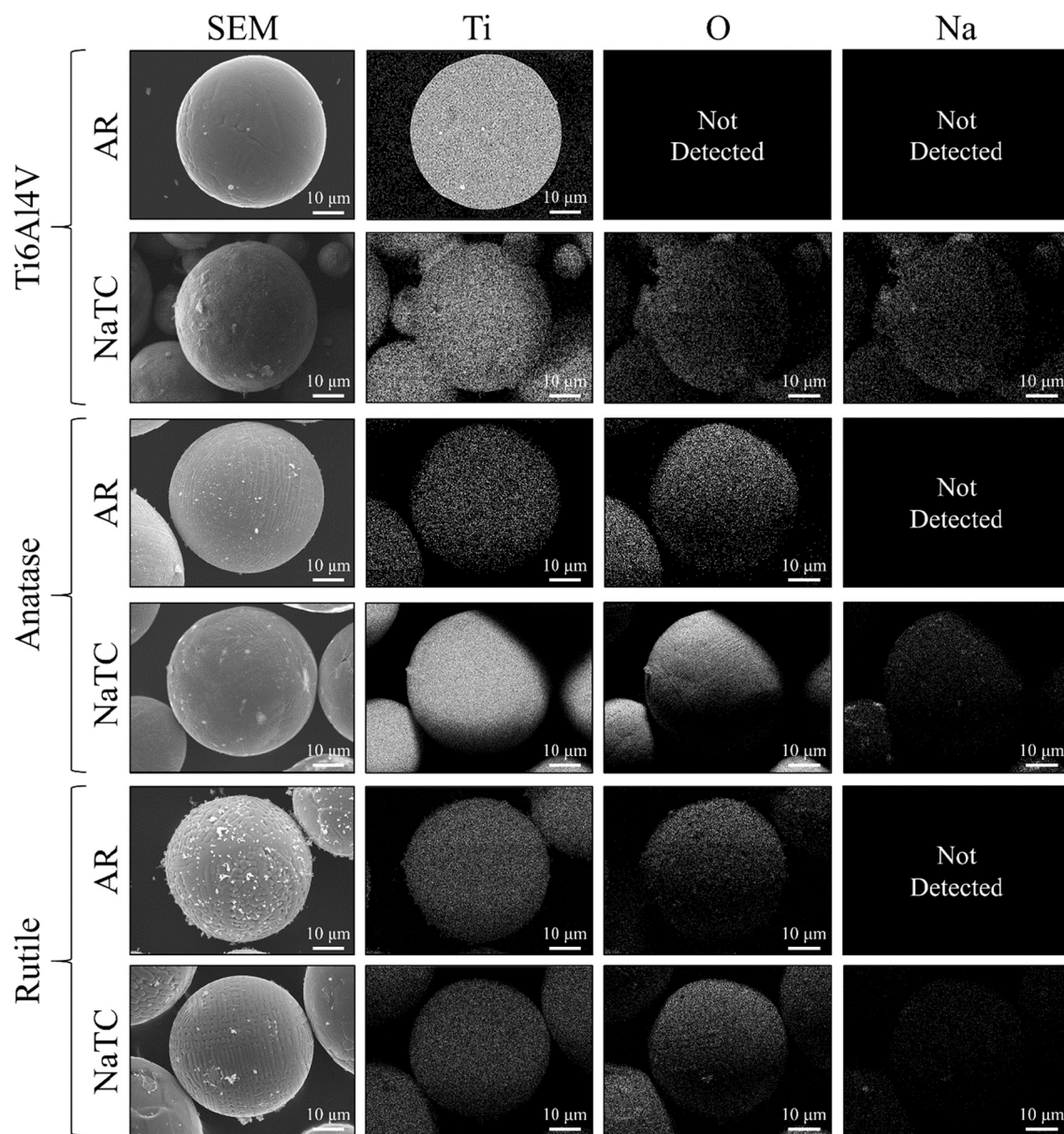
Fig. 6. EDS mapping of Ti6Al4V_MS, FS_Anatase_MS, and FS_Rutile_MS samples, with their NaTC counterparts, demonstrating homogeneous distribution of Ti, O and Na, where applicable, with relative elemental ratios due to count intensities. AR = as received prior to titanate conversion; NaTC = titanate converted.

3.3. XRD

Fig. 8 shows powder X-ray diffractograms for Ti6Al4V_MS, FS_Anatase_MS and FS_Rutile_MS as well as their corresponding titanate counterparts (Ti6Al4V_MS NaTC, FS_Anatase_MS NaTC and FS_Rutile_MS NaTC respectively). The X-ray diffractograms for both the FS_Anatase_MS and FS_Anatase_MS NaTC samples revealed that, as expected due to the conversion *via* flame-spheroidisation, rutile was the major phase (98–99 wt%) along with a smaller fraction of anatase (1–2 wt%). The FS_Anatase_MS NaTC diffractogram exhibited no evidence of any crystalline titanate reflections. The FS_Rutile_MS and FS_Rutile_MS NaTC X-ray diffractograms were broadly similar to the FS_Anatase_MS and FS_Anatase_MS NaTC diffraction patterns, and rutile was the principal phase along with a smaller fraction of anatase. The FS_Rutile_MS was comprised of approximately 2–3 wt% anatase and 97–98 wt% rutile. However, whist the FS_Rutile_MS NaTC diffractogram exhibited no definitive peaks which can be indexed to crystalline titanate, there were

several unidentified reflections situated at ~25, 38 and 54° 2θ, which appeared following the titanate conversion. The lattice parameters of the phases in the FS_Anatase_MS, FS_Rutile_MS, FS_Anatase_MS NaTC and FS_Rutile_MS NaTC samples were determined by Rietveld analysis and are reported in Table 4. This table showed that the titanate conversion had little to no effect on the lattice parameters of both the anatase and rutile phases.

The X-ray diffractogram from the Ti6Al4V_MS revealed a HCP α-Ti solid solution as the only indexable phase. The broad and somewhat complex nature of these reflections can be attributed to the rapid solidification rates associated with plasma atomisation. Likewise, only HCP α-Ti reflections were observed in the Ti6Al4V_MS NaTC diffractogram and there were no significant evidence of any crystalline titanate. The lattice parameters of these samples are also reported in Table 4, and the titanate conversion appeared to cause a very slight shift in the lattice parameters of the α-Ti phase.
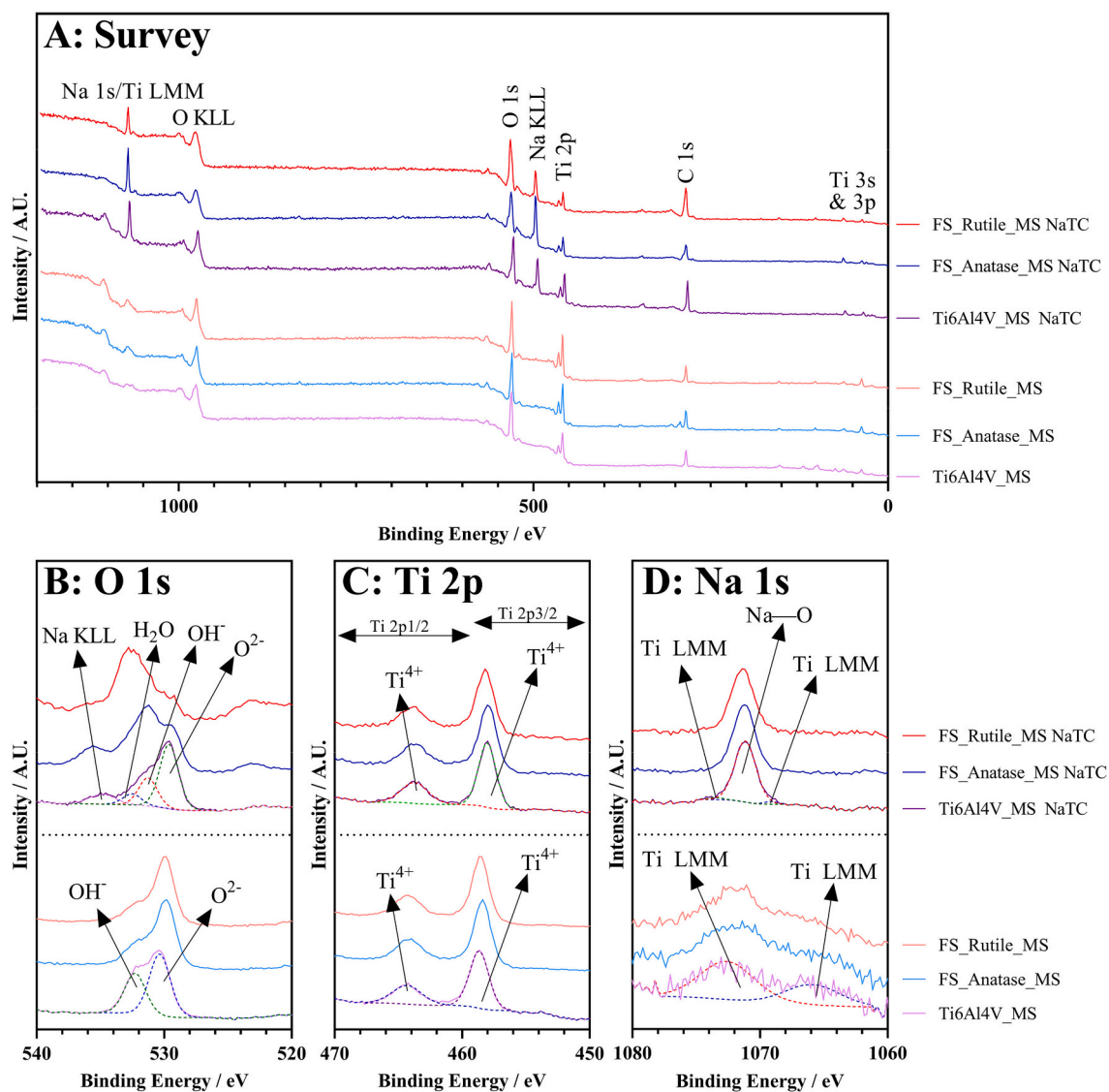
Fig. 7. X-ray photoelectron spectral analysis for as-prepared (Ti6Al4V_MS; FS_Anatase_MS; FS_Rutile_MS), and titanate converted Ti6Al4V (Ti6Al4V_MS NaTC) and TiO$_2$ (anatase – FS_Anatase_MS NaTC; rutile – FS_Rutile_MS NaTC) microspheres. (A) Survey spectra identifying all elemental photoelectron emissions, (B) High-resolution spectra of O 1s peaks with overlapping Na KLL Auger emission, (C) High-resolution spectra of Ti 2p doublet splitting peaks, and (D) High resolution spectra of Na 1s, with overlapping Ti LMM Auger emissions.

3.4. Raman spectroscopy

Raman spectral analysis is detailed in Fig. 9. Both rutile and anatase flame-spheroidised powders (FS_Rutile_MS and FS_Anatase_MS, respectively) demonstrated similar bands, even when subjected to titanate conversion. Bands were located at *ca.* 150, 230, 420, and 600 cm^{-1} corresponding to both anatase and rutile species. Specifically, the 150 cm^{-1} peak related to anatase B$_{1g}$ and E$_g$ modes, whilst the bands at *ca.* 230, 420, and 600 cm^{-1} correlated with rutile second order phonons (Ti$_2$O$_3$), E$_g$, and A$_{1g}$ modes, respectively. No titanate modes were noted.

For the Ti6Al4V powders however, significant dissimilarities were noted pre- and post-titanate conversion. The Ti6Al4V_MS powder did not present any noticeable modes, likely due to not being particularly Raman active. Following NaOH treatment, peaks at *ca.* 285, 440, and 920 cm^{-1}, with broad peaks around 680–800 cm^{-1} were seen, and were consistent with sodium hydrogen titanate (Na$_x$H$_{2-x}$Ti$_3$O$_7$).

3.5. Mercury porosimetry

Fig. 10 & Table 5 demonstrates the porosity measurements generated

via mercury porosimetry for the pre- and post-titanate converted samples. It is clear from the data that the most significant change in surface porosity was from the Ti6Al4V microspheres before and after the NaOH treatment, with porosities of *ca.* 31.7 and 60.1%, respectively. This highlighted sub-micron scale pores present on the surface due to the titanate conversion.

Higher cumulative intrusion (Fig. 10A) was seen in the titanate converted samples, compared to the unconverted counterparts, although the anatase and rutile flame-spheroidised, titanate-converted samples did not experience as significant increases as seen in the Ti6Al4V_MS NaTC sample. Furthermore, the log differential intrusion data (Fig. 10B and C) demonstrated higher incidences of small, sub-micron and nanometre-sized pores in the Ti6Al4V_MS NaTC sample compared to its unconverted counterpart, which only exhibited a sharp peak at *ca.* 10 μm, which is likely the interparticulate distance. In addition to this, the size of the interparticulate distance appears to broaden in the Ti6Al4V_MS NaTC.

The packing porosity of the pre-converted microspheres (Ti6Al4V_MS, FS_Rutile_MS, and FS_Anatase_MS) was found to be *ca.* 31.7, 43.8, and 43.4%, respectively, which is from the interparticulate

Table 2

XPS analysis of titanate converted (_MS NaTC) and non-titanate (_MS) converted Ti6Al4V and TiO_2 microspheres.

Sample code	Elements	Binding energy / eV	Corresponding bonds (area / %)	Ref.
Ti6Al4V_MS	O 1s	530.3 (O^{2-})	M^{x+}—O (60.54)	[39,40]
		532.3 (OH^-_t)	M^{x+}—OH (39.46)	
	Ti 2p 3/2	458.7 (Ti^{4+})	O—Ti^{4+} (100)	[39]
Ti6Al4V_MS NaTC	O 1s	529.6 (O^{2-})	Ti^{4+}—O (54.70)	[40]
		531.3 (OH^-_{br})	Ti^{4+}—OH (24.04)	
		532.5 (OH^-_t/H_2O)	O—H (9.44)	
		534.9 (Na KLL)	- (11.82)	
	Ti 2p 3/2	458.0 (Ti^{4+})	O—Ti^{4+} (100)	[23,24,41–43]
	Na 1s	1071.1	O—Na (95.2)	[23,24,41–44]
FS_Anatase_MS	O 1s	529.9 (O^{2-})	Ti^{4+}—O (73.56)	[39,40]
		532.2 (OH^-_t)	Ti—OH (26.44)	
	Ti 2p 3/2	458.4 (Ti^{4+})	O—Ti^{4+} (100)	[39]
FS_Anatase_MS NaTC	O 1s	529.4 (O^{2-})	Ti^{4+}—O (28.12)	[40]
		531.2 (OH^-_{br})	Ti^{4+}—OH (38.31)	
		532.8 (OH^-_t/H_2O)	O—H (17.12)	
		535.5 (Na KLL)	- (16.45)	
	Ti 2p 3/2	458.0 (Ti^{4+})	O—Ti^{4+} (100)	[23,24,41–43]
	Na 1s	1071.2	O—Na (81.4)	[23,24,41–44]
FS_Rutile_MS	O 1s	529.9 (O^{2-})	Ti^{4+}—O (78.19)	[39,40]
		532.2 (OH^-_t)	Ti—OH, $Ti^{2+/3+}$—O (21.81)	
	Ti 2p 3/2	458.6 (Ti^{4+})	O—Ti^{4+} (100)	[39]
FS_Rutile_MS NaTC	O 1s	529.6 (O^{2-})	Ti^{4+}—O (16.84)	[40]
		531.6 (OH^-_{br})	Ti^{4+}—OH (31.22)	
		533.0 (OH^-_t/H_2O)	O—H (44.95)	
		535.6 (Na KLL)	- (7.00)	
	Ti 2p 3/2	458.2 (Ti^{4+})	O—Ti^{4+} (100)	[23,24,41–43]
	Na 1s	1071.2	O—Na (83.2)	[23,24,41–44]

Table 3

Elemental composition analysis (at.%) as confirmed *via* XPS analysis of survey spectra. Data presented is the software calculated mean and standard deviation from CasaXPS.

Sample ID	Elemental composition / at.%		
	Na	O	Ti
Ti6Al4V_MS	0	84.4 ± 0.4	15.6 ± 0.4
Ti6Al4V_MS NaTC	17.6 ± 0.8	66.8 ± 0.9	15.6 ± 0.6
FS_Anatase_MS	0	77.6 ± 0.5	22.4 ± 0.5
FS_Anatase_MS NaTC	16.5 ± 0.4	73.4 ± 0.4	10.2 ± 0.3
FS_Rutile_MS	0	75.5 ± 0.4	24.5 ± 0.4
FS_Rutile_MS NaTC	9.5 ± 0.4	83.9 ± 0.5	6.7 ± 0.3

gaps, which are 'seen' as pores through the mercury porosimetry analysis. No significant variations were seen for the rutile and anatase microspheres post-conversion (Rutile_MS NaTC and Anatase_MS NaTC), highlighting no morphological changes due to the titanate conversion. All samples exhibited an increase in porosity values, however, the titanate converted rutile and anastase samples exhibited a significantly lower increase in porosity (9.0 and 5.4%, respectively), compared to the titanate converted Ti6Al4V microspheres (47.3%), relative to the unconverted samples (Fig. 10D).
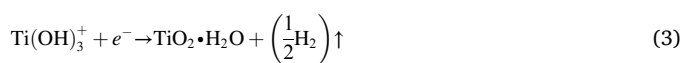
4. Discussion

Within the literature presently, there have been limited investigations into the usage of Ti-containing microspherical substrate being converted into titanate, with the view to understand the variation in relative surface area, compared to polished discs previously seen in the literature [23,45–47]. The authors postulate that through usage of microspheres, which have a titanate-converted top layer, may aid in water treatment and biomedical fields due to the increase in surface porosity, and ion-exchange potential. Kokubo et al. studied the mechanism of titanate formation on commercially pure Ti (Cp-Ti) substrates and demonstrated that the process was diffusion dependant, with movement of Na and O into the substrate to allow subsequent formation. This was achieved on both Cp-Ti, as well as many alloy types, including Gum metal (Ti-36Nb-2Ta-3Zr-0.3O) [47,48]. The most notable paper by

Xie et al., details the formation mechanism of titanate nanotubes using TiO_2 precursor materials, however, their formation occurred through hydrothermal methods at much higher temperatures (200 °C) than the present lower temperature (60 °C) methodology [49]. As such, it was interesting to compared the potential formation of nanoporous titanate films onto Ti6Al4V and TiO_2 microspherical substrates, at lower temperatures seen for titanate-converted TiO_2 literature thus far.

The generally agreed consensus on wet-chemical alkaline titanate formation, as detailed previously in Section 1 from the seminal papers by Kim et al. [23] and Kokubo [32], states that initially the TiO_2 passivated layer on the surface of Ti/Ti alloys is partially dissolved due to corrosive attack of hydroxyl groups.

$$TiO_2 + OH^- \rightarrow HTiO_3^- \tag{1}$$

Concurrently, the underlying Ti metal is hydrated *via* diffusion:

$$Ti + 3OH^- \rightarrow Ti(OH)_3^+ + 4e^- \tag{2}$$

$$Ti(OH)_3^+ + e^- \rightarrow TiO_2 \cdot H_2O + \left(\frac{1}{2}H_2\right)\uparrow \tag{3}$$

$$Ti(OH)_3^+ + OH^- \leftrightarrow Ti(OH)_4 \tag{4}$$

Consequently, the hydrated TiO_2 formed from the aforementioned reactions generates negatively charged titanium oxide hydrates.

$$TiO_2 \cdot nH_2O + OH^- \leftrightarrow HTiO_3^- \cdot nH_2O \tag{5}$$

Since these structures are negatively charged, combination with alkali ions in solution occurs, which in the case of NaOH is Na^+ to form sodium (hydrogen) titanate structures. However, to what extent this dependence on O has on the formation of titanate has yet to be quantified fully. This study outlined insights into this part of the titanate mechanism, through the production of Ti6Al4V microspheres (Ti6Al4V_MS), as well as those comprised of TiO_2 (anatase and rutile flame-spheroidised powders; FS_Anatase_MS and FS_Rutile_MS, respectively). Comparison of the morphological, structural, and chemical properties of these materials pre- and post-titanate conversion has enabled further insights into the role of O in the titanate mechanism to be gleaned.
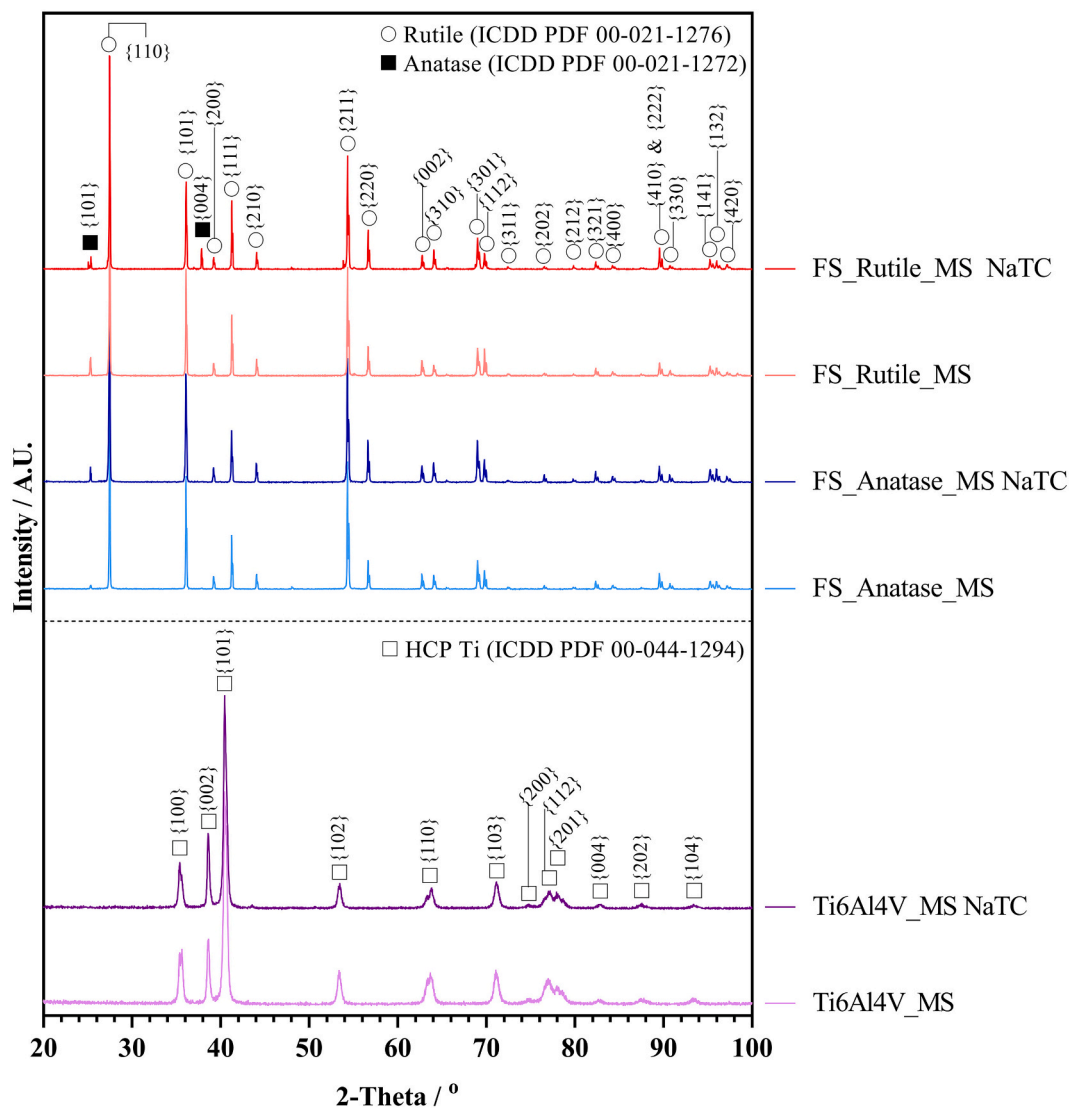
Fig. 8. XRD spectra for pre- and post-titanate converted samples. Peaks we identified as either HCP Ti (ICDD PDF 00-044-1294), Rutile (00-021-1276), or Anatase (00-021-1272).

Table 4

Lattice parameters of the known phases identified in the Ti6Al4V_MS, FS_Anatase_MS, FS_Rutile_MS, Ti6Al4V_MS NaTC, FS_Anatase_MS NaTC and FS_Rutile_MS NaTC as determined by Rietveld analysis.

Sample ID	Anatase lattice parameter (nm)		Rutile lattice parameter (nm)		Hcp α–Ti lattice parameter (nm)	
	a = b	c	a = b	c	a = b	c
Ti6Al4V_MS	0.3785	0.9518	0.4593	0.2960	–	–
Ti6Al4V_MS NaTC	0.3784	0.9518	0.4593	0.2960	–	–
FS_Anatase_MS	0.3788	0.9516	0.4594	0.2960	–	–
FS_Anatase_MS NaTC	0.3787	0.9514	0.4594	0.2960	–	–
FS_Rutile_MS	–	–	–	–	0.2924	0.4660
FS_Rutile_MS NaTC	–	–	–	–	0.2928	0.4668

From the data collected in this study, the authors present two potential factors that will serve as an extension to the currently accepted mechanism, providing a more comprehensive understanding of the wet-chemical alkaline titanate methodology. These factors are:

1) Inhibition of oxygen diffusion, oxygen vacancies/Ti interstitials and lower corrosion rate/reactivity in TiO_2 compared to Ti alloys, despite both containing a top surface containing TiO_2 (requirement for initiation of titanate formation).

2) Lack of free Ti in the TiO_2 materials preventing subsequent reactions to occur.

These factors, the data that suggests them, and their relation to the titanate formation mechanism, are described in detail below, as well as details regarding the microspherical nature of the substrates.

4.1. Oxygen diffusion, vacancies and diffusion barriers

It was evident that oxygen played a significant role in the conversion of titanate, with excessive quantities resulting in minimal titanate conversion (see SEM; Fig. 2 & Fig. 3). From the Kim et al. mechanism [23], titanate formation was reliant on a thin passivated TiO_2 layer forming on the top of the Ti-containing substrate, in which this layer facilitated the initial growth of the titanate structure through corrosive attack and diffusion of Na. Once the growth began to occur, this TiO_2 layer, and hydrate derivatives thereof, converted into sodium titanate (Fig. 11). The nanoporosity of this layer enhances diffusion of O^{2-} and Na^+ into
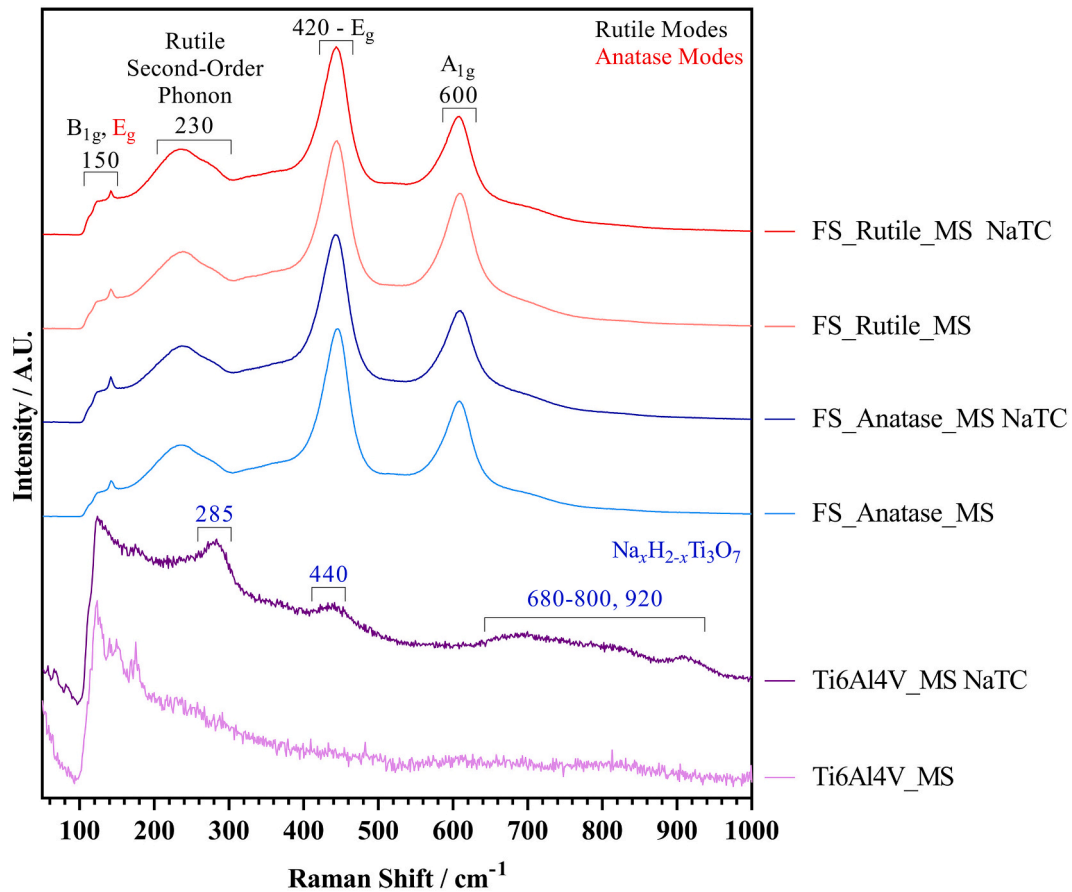
Fig. 9. Raman spectra of Ti6Al4V, as well as flame-spheroidised rutile and anatase samples pre- (_MS suffix) and post-titanate conversion (_MS NaTC suffix) using a 660 nm laser.

the underlying Ti material, as well as facilitating additional corrosive attack, forming further TiO₂ derivatives, which subsequently convert into sodium titanate. There is a limitation on the thickness of the titanate produced since this mechanism is reliant on diffusion of Na⁺ and O²⁻, which ultimately is thickness dependant; Fick's law of diffusion states that the rate of diffusion for a substance is proportional to both the surface area and concentration gradient and is inversely proportional to the thickness of the membrane/substrate which the diffusing substance is diffusing into [50]. Although O^{2-} can penetrate further (*ca.* 2 μm [43,51]) into the Ti surface through heat treatments, the process is limited by the initial O^{2-} and Na^+ diffusion, which reaches equilibrium at *ca.* 1 μm, hence the titanate thickness is limited to this [45].

By producing a purely TiO₂ surface, the middle aforementioned reactions (Eqs. (2)–(4)) cannot occur since there is no free Ti available to generate such species, although conversion can still occur *via* the first equation at the top surface as there is TiO₂ available to convert, albeit with a lower corrosion rate. Further growth and conversion of the titanate structure can, therefore, not be facilitated, and hence, is not seen in the TiO₂ microspheres (aside from the XPS analysis (Fig. 7), which investigated the top *ca.* 5 nm of the surface). Furthermore, diffusivity of O^{2-} was hindered due to the formation of TiO₂, as this layer can act as a barrier to O^{2-}, since any free lattice vacancy sites (such as the octahedral interstitial sites), now occupied by O^{2-}, are regarded as immobile blocking sites [52,53]. From Ouyang et al., the diffusivity of oxygen in α-Ti, β-Ti and TiO₂ was examined [54]. Diffusivity, being the rate of diffusion of one substance through another [55], as defined by:

$$D_A = Ae^{-\left(\frac{E}{RT}\right)} \tag{6}$$

where: D_A is the rate of species *A* diffusing through the reaction interface, *A* is the pre-exponential factor derived empirically, *E* is the activation energy of oxidation (J·mol⁻¹), *T* is the temperature (K) and *R* is the molar gas constant (8.314 J·K⁻¹·mol⁻¹) [54]. Ouyang et al.'s study derived expressions for O^{2-} diffusion (pure O_2 atmosphere) in α-Ti (HCP; Eq. (7)), β-Ti (BCC; Eq. (8)) and TiO₂ (rutile) (Eq. (9)):

$$D_\alpha\left(m^2 \cdot s^{-1}\right) = 7.78 \times 10^{-5} e\left(-\frac{203400}{RT}\right) \tag{7}$$

$$D_\beta\left(m^2 \cdot s^{-1}\right) = 3.3 \times 10^{-2} e\left(-\frac{246000}{RT}\right) \tag{8}$$

$$D_{TiO_2}\left(m^2 \cdot s^{-1}\right) = 1.7 \times 10^{-6} e\left(-\frac{276000}{RT}\right) \tag{9}$$

Assuming the diffusion mechanism obeys Arrhenius kinetics, the diffusivity of O^{2-} in α-Ti and TiO₂ at the temperature used in this study (333*K*) for titanate synthesis is 9.65×10^{-37} and 8.62×10^{-50} m²·s⁻¹, respectively. This substantial reduction in O^{2-} diffusion through TiO₂ relative to α–Ti demonstrates that one of the significant pathways for this mechanism is impeded, and therefore will inhibit titanate formation significantly compared to pure Ti or Ti alloys; this is exemplified in the SEM (Fig. 2, Fig. 3 & Fig. 5), EDS (Fig. 6) and XPS (Fig. 7) results gleaned. Results are discussed further in Section 4.3.

It is widely known that TiO₂ is a non-stoichiometric compound (usually denoted as TiO₂₋δ), and hence requires additional considerations when attempting to model diffusion kinetics of various species. As detailed by Das et al. [56], defects in the TiO₂ structure include the presence of oxygen vacancies $[V_O]$, as well as Ti interstitials $[Ti_i]$. Depending on different morphologies of TiO₂, variations in the
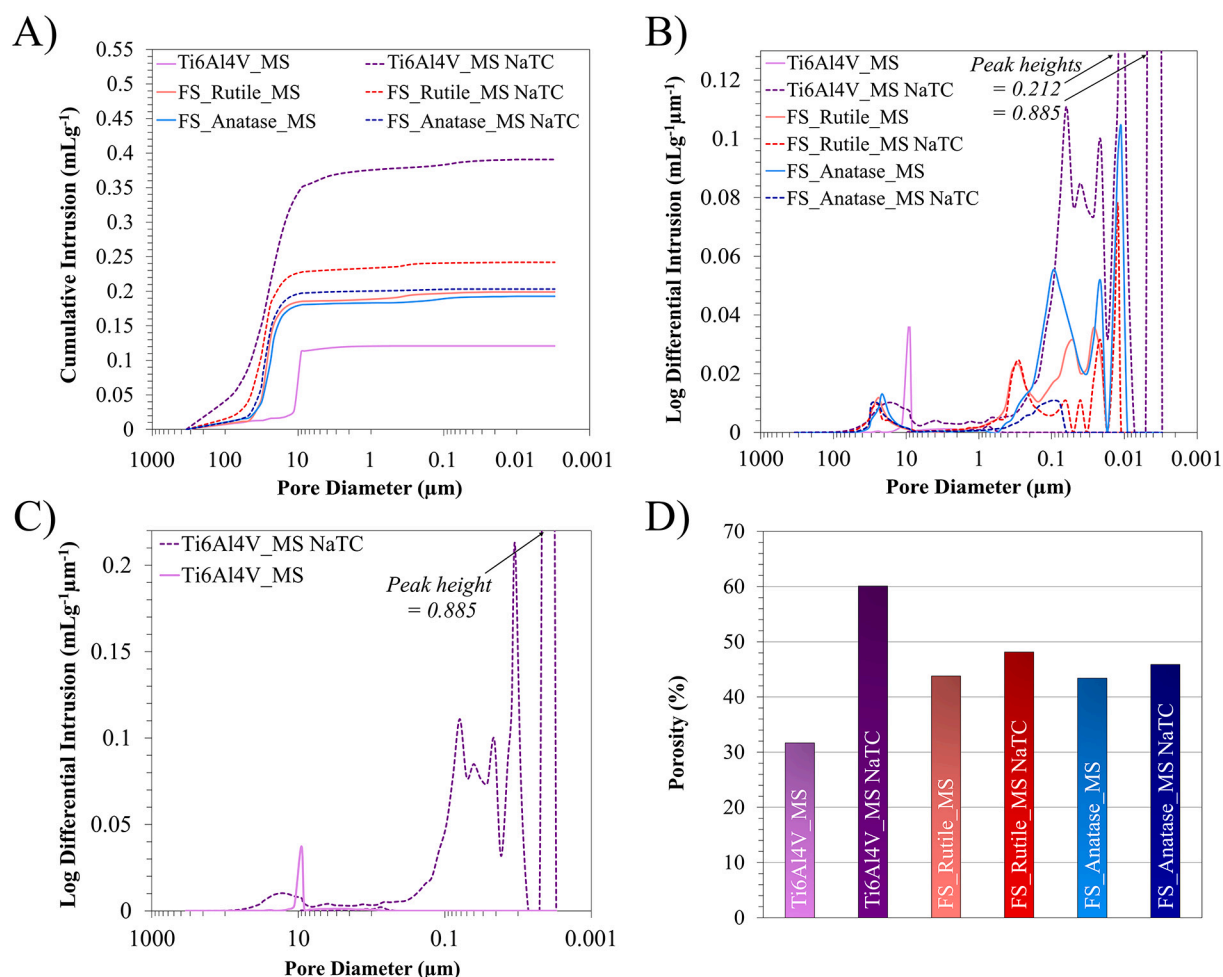
Fig. 10. Porosity properties of Ti6Al4V, rutile and anatase flame-spheroidised microspheres pre- and post-titanate conversion. A) Cumulative mercury intrusion curves *vs.* pore diameter (μm); B) Log differential intrusion curves of all samples demonstrating the porosity of the surfaces, in addition to interparticle voids; C) Log differential intrusion curves focussing on purely the Ti6Al4V pre- and post-titanate samples, illustrating the significant difference in porosity due to conversion; D) Porosity (%) of all samples obtained both pre- and post-titanate conversion.

Table 5
Mercury porosimetry data, detailing the bulk and apparent skeletal density used to calculate the approximate porosity of the microspheres.

Sample ID	Bulk density (g/mL)	Skeletal density (g/mL)	% porosity (hg porosimetry)
Ti6Al4V_MS	2.622	3.837	31.7
Ti6Al4V_MS NaTC	1.539	3.857	60.1
FS_Anatase_MS	2.203	3.920	43.8
FS_Anatase_MS NaTC	1.990	3.837	48.1
FS_Rutile_MS	2.252	3.979	43.4
FS_Rutile_MS NaTC	2.259	4.175	45.9

concentration of oxygen vacancies can occur. Additional reports suggest that during hydrogenation of the TiO_2 lattice, oxygen vacancies are formed, as well as the potential creation of Ti interstitials, however, the latter is more probable under high annealing temperatures (>600 °C; at the rutile transformation temperature) [57]. Therefore, oxygen vacancies are more likely to form in the anatase structure of TiO_2, whilst Ti interstitials being more prevalent in rutile TiO_2 [58].

Relating the above to the potential titanate formation mechanism, since the formation is heavily reliant on diffusion kinetics for oxygen species, correlating the above principles on vacancies is necessary to have a better understanding of this process. As discussed by Dawson [59], diffusion rates generally tended to decrease in $BaTiO_3$ and $SrTiO_3$, albeit having higher diffusion in $SrTiO_3$, when the concentration of oxygen vacancies decreases. Inhibition of titanate formation would therefore be enhanced in TiO_2 materials, since both exhibit more rutile phases, which have a thermodynamic tendency to form Ti interstitials rather than oxygen vacancies. Any free Ti interstitials may react with the NaOH solution to form titanate structures, however, the diffusion of oxygen species would be inhibited, effectively stalling the reaction. Furthermore, as detailed by Grubova et al. [60], the role of oxygen vacancies strongly influences the reactivity of the surface. Specifically, the rutile TiO_2 (110) surface plane has many defects, with oxygen vacancies providing a significant portion. Combining the understanding from the data within this paper, and the current thinking regarding the mechanism in the literature, it is evident that in the TiO_2 microspheres, the higher incidence of Ti interstitials over oxygen vacancies in the bulk material; as well as the higher surface reactivity in the rutile TiO_2 (110) plane; demonstrates the lack of sodium titanate formation in the bulk material, with a very thin layer (10s of nm) of which is only discernable *via* XPS (Fig. 7).

4.2. Dependence on free Ti

Although significant, the diffusion of O^{2-} is not the only limiting parameter of the reaction presented. Once the TiO_2 surface has reacted with the NaOH solution to form the $HTiO_3^-$ ions, there is a requirement
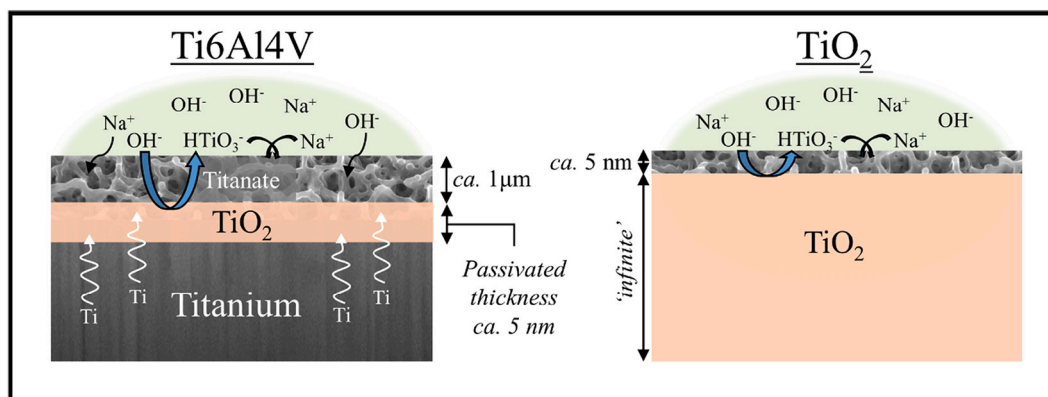
Fig. 11. Schematic diagram demonstrating titanate conversion as a result of substrate used; Ti6Al4V *vs.* TiO$_2$.

for hydration of the underlying Ti metal. This process must occur in the Ti6Al4V spheres, which are assumed to behave like bulk Ti due to the size of the spheres (> 20 μm) compared to the titanate thickness (*ca.* 1–1.6 μm), as well as previous reports demonstrating nanoporous sodium titanate layers can form on both Cp-Ti and Ti6Al4V; Al and V do not hinder this formation [33,61,62]. However, this process must be inhibited in the TiO$_2$ materials described. A postulate for this is presented in Xie et al.*'s* study [49], whereby different Ti-containing precursors were assessed on the formation of titanate nanowires through hydrothermal (200 °C) methods. They proposed that the mechanism occurs through a dissolution-crystallisation mechanism. The Ti contained within the substrate dissolves into the basic solution (NaOH), causing formation of $[Ti(OH)_4(OH_2)_2]^0$; similar species to those outlined in the mechanism above by Kim et al. [23]. Saturation occurs, which results in combination and formation of titanate structures, which nucleate on the surface. Subsequent diffusion, dissolution and formation occurs until a steady state is reached. This process occurred on Ti and TiO$_2$ (both reaching full conversion within 24 h), however, this was due to the differences in processing temperatures (200 *vs.* 60 °C). It is likely this process is impeded in TiO$_2$ due to the lower temperature employed in this study, hence reducing the potential diffusion and dissolution of free-Ti. Results exemplifying this factor are discussed in the section below (Section 4.3).

4.3. Combined evidence for the proposed mechanism factors

From the EDS and XPS analysis (Figs. 6 & 7), it was clear that trends in the oxygen, sodium and titanium content of the samples tested varied depending on the original composition, as well as the subsequent titanate conversion; the microspherical nature of the substrate did not seem to aid in titanate formation on the TiO$_2$ samples. From the Ti6Al4V samples, the data gathered agreed well with the hypothesis outlined above for the conversion of Ti6Al4V microspheres, compared to TiO$_2$. For the oxygen content following titanate conversion, the amount increased from *ca.* 0 to 61 at.% in EDS, whilst observing a reduction from *ca.* 88 to 67 at.% in XPS. The increase in O from EDS indicated there was a diffusion gradient occurring in the microspheres, akin to bulk Ti. A reduction in XPS is indicative of the relative ratio between the Ti, O and Na, since there is an increase in Na due to the titanate conversion. The Na content also increases for both EDS (*ca.* 0 to 5 at.%) and XPS (*ca.* 0 to 18 at.%), however, there was a higher quantity of Na in the XPS measurement, indicating a diffusion gradient, as illustrated by Kim et al. and Kokubo et al. [43,51]. Ti decreased in EDS (*ca.* 87 to 31 at.%), but remained constant in XPS (*ca.* 16 at.%), also indicating titanate conversion, and matching relative quantities from Zárate et al. [44], through the aforementioned mechanism.

In comparison to the FS_Anatase_MS and FS_Rutile_MS microspheres, and their titanate converted counterparts, the relative quantities of Na,

O, and Ti, were substantially different to the Ti6Al4V_MS samples. Oxygen content pre- and post-titanate conversion for both EDS and XPS, remained approximately constant: Anatase from *ca.* 70 to 68 at.% (EDS) and *ca.* 78 to 73 at.% (XPS); and Rutile from *ca.* 69 to 70 at.% (EDS) and *ca.* 76 to 84 at.% (XPS), for pre- (_MS) and post-titanate converted (_MS NaTC) samples, respectively. There were marginal changes to the surface composition (XPS), probably due to titanate conversion occurring in the top few nm of the surface, whilst the mean composition through the microsphere (*ca.* 2 μm; EDS) remained constant. For both the anatase and rutile flame-spheroidised samples (_MS/_MS NaTC), Na content increased significantly post-titanate conversion (NaTC) for the XPS measurements: *ca.* 0 to 17 at.% and 0 to 10 at.% for Anatase_MS (NaTC) and Rutile_MS (NaTC) samples, respectively, whilst EDS remained <1 at. % for both. This exemplified that the titanate conversion occurring in the top portion of the surface, however, was limited to just the surface, since low quantities are noted in EDS. A similar trend was seen for Ti, with similar values (*ca.* 30 at.%) detailed in EDS for both FS_Anatase_MS and FS_Rutile_MS pre- and post-titanate conversion, whilst the XPS values reduced for both: *ca.* 22 to 10 at.% and 25 to 7 at.% for FS_A-natase_MS NaTC and FS_Rutile_MS NaTC, respectively. This reduction is likely due to the top portion of the surface reacting with the NaOH solution to form the HTiO$_3^-$ species essential for the initial titanate formation, exemplifying the increase in Na and O content in XPS as a result. Once formed, and in agreement with the previously outlined hypothesis, this layer in conjunction with there being no free movement of Ti, resulted in the inhibition of the titanate mechanism. Thus, limiting titanate formation to the top few nanometres of the surface.

Additional bonding information, and insights into titanate formation were noted through X-ray diffraction and Raman spectral analyses (Figs. 8 & 9). For the anatase and rutile samples, both pre-and post-titanate conversion, only anatase and rutile bonding/phases were seen [63], which further demonstrated the limited formation of titanate on the oxygen-rich powders. The broad Raman peaks located at *ca.* 420 and 600 cm^{-1} are in agreement with Exarhos [64], which correspond to E$_g$ and A$_{1g}$ rutile modes that have the same localised structural groups with absence of long-range order. Additional anatase and rutile Raman bands located at *ca.* 150 and 230 cm^{-1} correlate with studies by Porto et al. [65] and Ocaña et al. [66], respectively, as well as the present authors [20,21]. The similarities in the powders is due to the high flame temperatures (>1500 °C) that occurred during the flame spheroidisation process [67] and the presence of oxygen causing extensive rutile formation, with residual anatase phases, matching the XRD analysis (Fig. 8) [68].

Conversely, the Ti6Al4V samples detailed titanate bonding, in agreement with EDS and XPS analyses (Figs. 6 & 7, respectively), albeit not seen in XRD due to the higher penetration depth, with Raman peaks located at *ca.* 285, 440, a broad peak at 860–800, and 900 cm^{-1} [69–71]. The peaks at *ca.* 285 and 900 cm^{-1} are in good agreement with

previous studies by the present authors, demonstrating either intrinsic hydrogen titanate ($H_2Ti_3O_7$) and/or $Na_2Ti_3O_7$ bands, similar to Rodrí-guez-González et al. [72] and Bamberger et al. [73], respectively. Furthermore, the peak located at *ca.* 440 cm^{-1}, indicated Ti—O bending vibrations of 6- and 3-coordinated Ti and O, respectively, which is in good agreement with Ma et al. [74] and Kim et al. [42]. The broad peak ranging from 680 to 800 cm^{-1}, is likely [TiO_6] octahedral Ti—O—Ti vibrations, which are characteristic of alkaline titanate structures [75,76]. Cumulatively, through understanding the reaction mechanism outlined, the diffusion processes occurring through these reactions, as well as data provided, it was clear how titanate growth was inhibited due to excessive O in the TiO_2 microspheres, and that there is a requirement for free Ti in order for further diffusion and conversion to proceed.

In addition to the chemical and morphological understanding of the conversion, mercury porosimetry analysis was also conducted (Fig. 10), to gain some insight of the surface porosity, and if titanate formation had occurred on the FS_Anatase_MS NaTC and FS_Rutile_MS NaTC samples, albeit not visible under standard microscopy. An increase of *ca.* 5–9% was seen in porosity from the FS_Anatase_MS and FS_Rutile_MS to FS_Anatase_MS NaTC and FS_Rutile_MS NaTC samples, however, the Ti6Al4V_MS to Ti6Al4V_MS NaTC transition exhibited a *ca.* 47% increase. This drastic increase was indicative of the increased roughness due to the characteristic nanoporosity of the titanate formation, and was in line with the log differential intrusion (Fig. 10B and C) and SEM micrographs (Fig. 2). Additionally, the interparticulate distance calculated to *ca.* 10–20 μm for the Ti6Al4V_MS exhibited a broadening (*ca.* 2–50 μm), which is likely due to the effect of titanate strut formation. The titanate structures have a significant effect on the interparticulate distance, due to interlocking of the struts reducing the distance in some case, whilst an increase in microsphere diameter (titanate coating thickness of *ca.* 800 nm results in an increase in microsphere diameter to at least 1.6 μm) due to the coating may have cause the variance at the upper bound.

Despite titanate formation occurring chemically, there was no morphological and porosity evidence seen in the SEM micrographs (Fig. 2 *vs.* Fig. 5) and the mercury porosimetry data (Fig. 10 & Table 5) of the TiO_2 (FS_Anatase_MS NaTC and FS_Rutile_MS NaTC) samples, which was linked to the growth of the sodium titanate nanocrystals due to the interplay of solution and substrate equilibrium reactions. Huang et al. hypothesised, and extended further than Kim et al., the likely mechanistic growth of titanate structures [77]. Additional work by Zhao et al. [78], Lu et al. [79], and Mao et al. [80] have all focussed on the growth mechanism of titanate structures, however, due to differences in the methodology, particularly the chemical routes used: Zhao [78] utilised 8.5 mL tetrabutyl titanate in HCl/Neutral/NaOH conditions; Lu [79] investigated combined bismuth/sodium titanate structures through bismuth nitrate pentahydrate, TiO_2 and a NaOH mineraliser; whilst Mao [80] focussed on the growth of titanate structures using combined H_2O_2/NaOH solutions, which enhanced oxidation, it was difficult to specifically comment with regard to the present study. The growth mechanism was dependent on the presence of a Ti/oxide interface. Due to the presence of NaOH, the oxide layer present will react to form $Na_{2-x}(H_x)TiO_3$ ($x = 1$ or 0), which occurs inhomogeneously across the surface. This resulted in localised areas of increased dissolution and conversion, which enabled exposure of Ti, and thus resulted in further oxidation and dissolution. In the case of TiO_2 (which was not observed by Huang et al. but of which the mechanism is hypothesised here), and despite inhomogeneous dissolution and conversion, the underlying layers were TiO_2 not Ti, and hence ultimately reached equilibrium once all of the underlying TiO_2 had converted to titanate, inhibiting further conversion. Furthermore, additional mechanisms involving the diffusion of OH$^-$ in high concentration NaOH solutions could cause bulk TiO_2 to react to form $Ti_3O_7^{2-}$, however, again this process was ultimately diffusion limited, and the absence of free Ti limited subsequent reactions [77].

5. Conclusions

As evidenced from the data, successful formation of a titanate layer was produced on the Ti6Al4V microspheres, as previously hypothesised. Conversely, the formation of TiO_2 microspheres using anatase and rutile powder, resulted in no morphological nanoporous titanate growth, however, evidence of titanate formation *via* chemical analysis only in the XPS results, indicated minimal surface formation. Residual Na (< 1 at.%) *via* EDS was found on both of these samples, however, the low quantity evidenced the limitation of titanate formation due to O content in the substrate. The titanate formation mechanism was proposed to be a culmination of the material present and the ability for ions to diffuse through the structure. In the Ti6Al4V samples, there is an intrinsic passivated TiO_2 layer that forms (*ca.* 5 nm thick) due to atmospheric exposure. This is fundamental to the initial formation of the sodium titanate structures. Subsequent growth is driven through conversion of TiO_2 into titanate, whilst facilitating Na and O diffusion into the Ti structure to continue its growth. This mechanism is limited to the depth of Na diffusion (*ca.* 1 μm from the literature). For the TiO_2 samples, Na and O are limited in their ability to diffuse into the material, since there is no free Ti available for conversion, therefore limiting the titanate growth only to the top surface.

Additional assessments by focussing on TiO_2 microspheres solely and varying the temperature and concentration of the NaOH solution should be conducted to a point where titanate formation occurs on the TiO_2 substrates as a separate study to the present publication. The applicability of the nanoporous sodium titanate structures onto microspherical substrates should certainly be investigated for biomedical, electro-catalysis, and water treatment applications, as well as comparing this to the state-of-the-art for that particular field. Some of which will be described in subsequent publications by the present authors.

Data availability

The raw/processed data required to reproduce these findings cannot be shared at this time as the data also forms part of an ongoing study.

Declaration of Competing Interest

The authors declare that they have no known competing financial interests or personal relationships that could have appeared to influence the work reported in this paper.

Acknowledgements

References

[1] S. Shen, C. Wang, M. Sun, M. Jia, Z. Tang, J. Yang, Free-standing sodium titanate ultralong nanotube membrane with oil-water separation, self-cleaning, and photocatalysis properties, Nanoscale Res. Lett. 15 (1) (2020) 22.

[2] T. Wen, Z. Zhao, C. Shen, J. Li, X. Tan, A. Zeb, X. Wang, A.-W. Xu, Multifunctional flexible free-standing titanate nanobelt membranes as efficient sorbents for the removal of radioactive 90 Sr 2+ and 137 Cs+ ions and oils, Sci. Rep. 6 (1) (2016) 1–10.

[3] M. Grandcolas, A. Louvet, N. Keller, V. Keller, Layer-by-layer deposited titanate-based nanotubes for solar photocatalytic removal of chemical warfare agents from textiles, Angew. Chem. Int. Ed. 48 (1) (2009) 161–164.

[4] T. Kokubo, H.-M. Kim, M. Kawashita, T. Nakamura, Bioactive metals: preparation and properties, J. Mater. Sci. Mater. Med. 15 (2) (2004) 99–107, https://doi.org/10.1023/B:JMSM.0000011809.36275.0c.

[5] D.J. Yang, Z.F. Zheng, H.Y. Zhu, H.W. Liu, X.P. Gao, Titanate nanofibers as intelligent absorbents for the removal of radioactive ions from water, Adv. Mater. 20 (14) (2008) 2777–2781.

[6] J. Liu, X. Wei, X.-W. Liu, Two-dimensional wavelike spinel lithium titanate for fast lithium storage, Sci. Rep. 5 (1) (2015) 1–6.

[7] D.V. Bavykin, F.C. Walsh, Kinetics of alkali metal ion exchange into nanotubular and nanofibrous titanates, J. Phys. Chem. C 111 (40) (2007) 14644–14651.

[8] V.D.A. Cardoso, A.G. de Souza, P.P. Sartoratto, L.M. Nunes, The ionic exchange process of cobalt, nickel and copper (II) in alkaline and acid-layered titanates, Colloids Surf. A Physicochem. Eng. Asp. 248 (1–3) (2004) 145–149.

[9] H. Izawa, S. Kikkawa, M. Koizumi, Ion exchange and dehydration of layered [sodium and potassium] titanates, Na2Ti3O7 and K2Ti4O9, J. Phys. Chem. 86 (25) (1982) 5023–5026.

[10] S. Liu, J. Xia, J. Yu, Amine-functionalized titanate nanosheet-assembled yolk@shell microspheres for efficient cocatalyst-free visible-light photocatalytic CO2 reduction, ACS Appl. Mater. Interfaces 7 (15) (2015) 8166–8175.

[11] H.M. Kim, F. Miyaji, T. Kokubo, T. Nakamura, Preparation of bioactive Ti and its alloys via simple chemical surface treatment, J. Biomed. Mater. Res. 32 (3) (1996) 409–417.

[12] Y. Mao, S.S. Wong, Size-and shape-dependent transformation of nanosized titanate into analogous anatase titania nanostructures, J. Am. Chem. Soc. 128 (25) (2006) 8217–8226.

[13] Z. Chang, J. Liu, J. Liu, X. Sun, Titanate nanosheets and nanotubes: alkalinity manipulated synthesis and catalyst support application, J. Mater. Chem. 21 (1) (2011) 277–282.

[14] R.V. Chernozem, M.A. Surmeneva, V.P. Ignatov, O.O. Peltek, A.A. Goncharenko, A. R. Muslimov, A.S. Timin, A.I. Tyurin, Y.F. Ivanov, C.R. Grandini, Comprehensive characterization of titania nanotubes fabricated on Ti–Nb alloys: surface topography, structure, physicomechanical behavior, and a cell culture assay, ACS Biomater. Sci. Eng. 6 (3) (2020) 1487–1499.

[15] S.K. Divakarla, S. Yamaguchi, T. Kokubo, D.-W. Han, J.H. Lee, W. Chrzanowski, Improved bioactivity of GUMMETAL®, Ti59Nb36Ta2Zr3O0. 3, via formation of nanostructured surfaces, J. Tissue Eng. 9 (2018) (2041731418774178).

[16] Y. Su, S. Komasa, T. Sekino, H. Nishizaki, J. Okazaki, Nanostructured Ti6Al4V alloy fabricated using modified alkali-heat treatment: characterization and cell adhesion, Mater. Sci. Eng. C 59 (2016) 617–623.

[17] S. Yamaguchi, S. Nath, Y. Sugawara, K. Divakarla, T. Das, J. Manos, W. Chrzanowski, T. Matsushita, T. Kokubo, Two-in-one biointerfaces—antimicrobial and bioactive nanoporous gallium titanate layers for titanium implants, Nanomaterials 7 (8) (2017) 229.

[18] A. Rodriguez-Contreras, D. Torres, J. Guillem-Marti, P. Sereno, M.P. Ginebra, J. A. Calero, J.M. Manero, E. Ruperez, Development of novel dual-action coatings with osteoinductive and antibacterial properties for 3D-printed titanium implants, Surf. Coat. Tech. 403 (2020), 126381.

[19] S.B. Lee, U. Otgonbayar, J.H. Lee, K.M. Kim, K.N. Kim, Silver ion-exchanged sodium titanate and resulting effect on antibacterial efficacy, Surf. Coat. Tech. 205 (2010) S172–S176.

[20] M.D. Wadge, B.W. Stuart, K.G. Thomas, D.M. Grant, Generation and characterisation of gallium titanate surfaces through hydrothermal ion-exchange processes, Mater. Des. 155 (2018) 264–277.

[21] M.D. Wadge, B. Turgut, J.W. Murray, B.W. Stuart, R.M. Felfel, I. Ahmed, D. M. Grant, Developing highly nanoporous titanate structures via wet chemical conversion of DC magnetron sputtered titanium thin films, J. Colloid Interface Sci. 566 (2020) 271–283.

[22] M.D. Wadge, J. McGuire, B.V.T. Hanby, R.M. Felfel, I. Ahmed, D.M. Grant, Tailoring the degradation rate of magnesium through biomedical nano-porous titanate coatings, J. Magnes. Alloy 9 (1) (2021) 336–350.

[23] H.M. Kim, F. Miyaji, T. Kokubo, T. Nakamura, Preparation of bioactive Ti and its alloys via simple chemical surface treatment, J. Biomed. Mater. Res. 32 (3) (1996) 409–417.

[24] T. Kokubo, F. Miyaji, H.M. Kim, T. Nakamura, Spontaneous formation of bonelike apatite layer on chemically treated titanium metals, J. Am. Ceram. Soc. 79 (4) (1996) 1127–1129.

[25] H. Eslami, F. Moztarzadeh, T.S.J. Kashi, K. Khoshroo, M. Tahriri, Hydrothermal synthesis and characterization of TiO2-derived nanotubes for biomedical applications, synthesis and reactivity in inorganic, Metal Organ. Nano Metal Chem. 46 (8) (2016) 1149–1156.

[26] G.-S. Kim, H.-K. Seo, V. Godble, Y.-S. Kim, O.-B. Yang, H.-S. Shin, Electrophoretic deposition of titanate nanotubes from commercial titania nanoparticles: application to dye-sensitized solar cells, Electrochem. Commun. 8 (6) (2006) 961–966.

[27] L. Torrente-Murciano, A.A. Lapkin, D. Chadwick, Synthesis of high aspect ratio titanate nanotubes, J. Mater. Chem. 20 (31) (2010) 6484–6489.

[28] A.-L. Papa, L. Dumont, D. Vandroux, N. Millot, Titanate nanotubes: towards a novel and safer nanovector for cardiomyocytes, Nanotoxicology 7 (6) (2012) 1131–1142.

[29] A.-L. Papa, J. Boudon, V. Bellat, A. Loiseau, H. Bisht, F. Sallem, R. Chassagnon, V. Bérard, N. Millot, Dispersion of titanate nanotubes for nanomedicine: comparison of PEI and PEG nanohybrids, Dalton Trans. 44 (2) (2015) 739–746.

[30] H. Zhao, W. Dong, Y. Zheng, A. Liu, J. Yao, C. Li, W. Tang, B. Chen, G. Wang, Z. Shi, The structural and biological properties of hydroxyapatite-modified titanate nanowire scaffolds, Biomaterials 32 (25) (2011) 5837–5846.

[31] H.-C. Hsu, S.-C. Wu, S.-K. Hsu, F.-W. Lin, W.-F. Ho, Fabrication and characterization of novel porous titanium microspheres for biomedical applications, Mater. Charact. 106 (2015) 317–323.

[32] T. Kokubo, Apatite formation on surfaces of ceramics, metals and polymers in body environment, Acta Mater. 46 (7) (1998) 2519–2527.

[33] S.S. Sayedain, A. Ekrami, M. Badrossamay, Production and characterization of Ti6Al4V/CaP nanocomposite powder for powder-based additive manufacturing systems, Powder Technol. 386 (2021) 319–334.

[34] C. Phutela, N.T. Aboulkhair, C.J. Tuck, I. Ashcroft, The effects of feature sizes in selectively laser melted Ti-6Al-4V parts on the validity of optimised process parameters, Materials 13 (1) (2020) 117.

[35] K.M.Z. Hossain, U. Patel, A.R. Kennedy, L. Macri-Pellizzeri, V. Sottile, D.M. Grant, B.E. Scammell, I. Ahmed, Porous calcium phosphate glass microspheres for orthobiologic applications, Acta Biomater. 72 (2018) 396–406.

[36] R. Young, The Rietveld Method, Oxford University Press, New York, 1993.

[37] R.W. Cheary, A. Coelho, A fundamental parameters approach to X-ray line-profile fitting, J. Appl. Crystallogr. 25 (2) (1992) 109–121.

[38] R.W. Cheary, A.A. Coelho, J.P. Cline, Fundamental parameters line profile fitting in laboratory diffractometers, J. Res. Natl. Inst. Stand. Technol. 109 (1) (2004) 1.

[39] U. Diebold, T. Madey, TiO2 by XPS, Surf. Sci. Spectra 4 (3) (1996) 227–231.

[40] P. Krishnan, M. Liu, P.A. Itty, Z. Liu, V. Rheinheimer, M.-H. Zhang, P.J. Monteiro, E.Y. Liya, Characterization of photocatalytic TiO2 powder under varied environments using near ambient pressure X-ray photoelectron spectroscopy, Sci. Rep. 7 (2017) 43298.

[41] J.F. Moulder, W.F. Stickle, P.E. Sobol, K.D. Bomben, Handbook of X-ray Photoelectron Spectroscopy: A Reference Book of Standard Spectra for Identification and Interpretation of XPS Data, Perkin-Elmer Co., Minnesota, U.S.A, 1995.

[42] H.M. Kim, F. Miyaji, T. Kokubo, T. Nakamura, Effect of heat treatment on apatite-forming ability of Ti metal induced by alkali treatment, J. Mater. Sci. Mater. Med. 8 (6) (1997) 341–347.

[43] H.M. Kim, F. Miyaji, T. Kokubo, S. Nishiguchi, T. Nakamura, Graded surface structure of bioactive titanium prepared by chemical treatment, J. Biomed. Mater. Res. A 45 (2) (1999) 100–107.

[44] R.A. Zarate, S. Fuentes, A.L. Cabrera, V.M. Fuenzalida, Structural characterization of single crystals of sodium titanate nanowires prepared by hydrothermal process, J. Cryst. Growth 310 (15) (2008) 3630–3637.

[45] T. Kokubo, S. Yamaguchi, Novel bioactive titanate layers formed on Ti metal and its alloys by chemical treatments, Materials 3 (1) (2010) 48–63.

[46] T. Kizuki, T. Matsushita, T. Kokubo, Antibacterial and bioactive calcium titanate layers formed on Ti metal and its alloys, J. Mater. Sci. Mater. Med. 25 (7) (2014) 1737–1746.

[47] S. Yamaguchi, T. Kizuki, H. Takadama, T. Matsushita, T. Nakamura, T. Kokubo, Formation of a bioactive calcium titanate layer on gum metal by chemical treatment, J. Mater. Sci. Mater. Med. 23 (4) (2012) 873–883.

[48] M. Tanaka, M. Takemoto, S. Fujibayashi, T. Kawai, S. Yamaguchi, T. Kizuki, T. Matsushita, T. Kokubo, T. Nakamura, S. Matsuda, Bone bonding ability of a chemically and thermally treated low elastic modulus Ti alloy: gum metal, J. Mater. Sci. Mater. Med. 25 (3) (2014) 635–643.

[49] J. Xie, X. Wang, Y. Zhou, Understanding formation mechanism of titanate nanowires through hydrothermal treatment of various Ti-containing precursors in basic solutions, J. Mater. Sci. Technol. 28 (6) (2012) 488–494.

[50] Y.-Y. Won, D. Ramkrishna, Revised formulation of Fick's, Fourier's, and Newton's laws for spatially varying linear transport coefficients, ACS Omega 4 (6) (2019) 11215–11222.

[51] T. Kokubo, T. Matsushita, H. Takadama, T. Kizuki, Development of bioactive materials based on surface chemistry, J. Eur. Ceram. Soc. 29 (7) (2009) 1267–1274.

[52] H. Nakajima, M. Koiwa, Diffusion in titanium, ISIJ Int. 31 (8) (1991) 757–766.

[53] R. Schaub, E. Wahlstrom, A. Ronnau, E. Lagsgaard, I. Stensgaard, F. Besenbacher, Oxygen-mediated diffusion of oxygen vacancies on the TiO2(110) surface, Science 299 (5605) (2003) 377–379.

[54] P. Ouyang, G. Mi, P. Li, L. He, J. Cao, X. Huang, Non-isothermal oxidation behavior and mechanism of a high temperature near-alpha titanium alloy, Materials 11 (11) (2018) 2141.

[55] H. Mehrer, Diffusion in Solids: Fundamentals, Methods, Materials, Diffusion-controlled Processes, Springer Science & Business Media, 2007.

[56] T.K. Das, P. Ilaiyaraja, P.S. Mocherla, G. Bhalerao, C. Sudakar, Influence of surface disorder, oxygen defects and bandgap in TiO2 nanostructures on the photovoltaic properties of dye sensitized solar cells, Sol. Energy Mater. Sol. Cells 144 (2016) 194–209.

[57] A. Naldoni, M. Allieta, S. Santangelo, M. Marelli, F. Fabbri, S. Cappelli, C. L. Bianchi, R. Psaro, V. Dal Santo, Effect of nature and location of defects on bandgap narrowing in black TiO2 nanoparticles, J. Am. Chem. Soc. 134 (18) (2012) 7600–7603.

[58] B.J. Morgan, G.W. Watson, Intrinsic n-type defect formation in TiO2: a comparison of rutile and anatase from GGA+ U calculations, J. Phys. Chem. C 114 (5) (2010) 2321–2328.

[59] J.A. Dawson, Dynamical insights into oxygen diffusion in BaTiO3 and SrTiO3, Phys. Status Solid. B 257 (1) (2020) 1900422.

[60] I.Y. Grubova, M.A. Surmeneva, S. Huygh, R.A. Surmenev, E.C. Neyts, Density functional theory study of interface interactions in hydroxyapatite/rutile composites for biomedical applications, J. Phys. Chem. C 121 (29) (2017) 15687–15695.

[61] M. Goto, A. Matsumine, S. Yamaguchi, H. Takahashi, K. Akeda, T. Nakamura, K. Asanuma, T. Matsushita, T. Kokubo, A. Sudo, Osteoconductivity of bioactive Ti-

6Al-4V implants with lattice-shaped interconnected large pores fabricated by electron beam melting, J. Biomater. Appl. 35 (9) (2021) 1153–1167.

[62] A. Rajendran, S. Sugunapriyadharshini, D. Mishra, D.K. Pattanayak, Role of calcium ions in defining the bioactivity of surface modified Ti metal, Mater. Sci. Eng. C 98 (2019) 197–204.

[63] J. He, Y.-e. Du, Y. Bai, J. An, X. Cai, Y. Chen, P. Wang, X. Yang, Q. Feng, Facile formation of anatase/rutile TiO2 nanocomposites with enhanced photocatalytic activity, Molecules 24 (16) (2019) 2996.

[64] G.J. Exarhos, High temperature Raman studies of phase transitions in thin film dielectrics, in: MRS Online Proceedings Library (OPL) 48, 1985.

[65] S. Porto, P. Fleury, T. Damen, Raman spectra of TiO2, MgF2, ZnF2, FeF2, and MnF2, Phys. Rev. 154 (2) (1967) 522.

[66] M. Ocana, J.V. Garcia-Ramos, C.J. Serna, Low-temperature nucleation of rutile observed by Raman spectroscopy during crystallization of TiO2, J. Am. Ceram. Soc. 75 (7) (1992) 2010–2012.

[67] J.M. Díaz, S.A. Samad, E. Steer, N. Neate, H. Constantin, M.T. Islam, P.D. Brown, I. Ahmed, Flame spheroidisation of dense and porous Ca 2 Fe 2 O 5 microspheres, Mater. Adv. 1 (9) (2020) 3539–3544.

[68] D.A.H. Hanaor, C.C. Sorrell, Review of the anatase to rutile phase transformation, J. Mater. Sci. 46 (4) (2011) 855–874.

[69] V. Prabu, P. Karthick, A. Rajendran, D. Natarajan, M.S. Kiran, D.K. Pattanayak, Bioactive Ti alloy with hydrophilicity, antibacterial activity and cytocompatibility, RSC Adv. 5 (63) (2015) 50767–50777.

[70] T. Kizuki, H. Takadama, T. Matsushita, T. Nakamura, T. Kokubo, Effect of Ca contamination on apatite formation in a Ti metal subjected to NaOH and heat treatments, J. Mater. Sci. Mater. Med. 24 (3) (2013) 635–644.

[71] D.K. Pattanayak, T. Kawai, T. Matsushita, H. Takadama, T. Nakamura, T. Kokubo, Effect of HCl concentrations on apatite-forming ability of NaOH–HCl-and heat-treated titanium metal, J. Mater. Sci. Mater. Med. 20 (12) (2009) 2401–2411.

[72] V. Rodríguez-González, S. Obregón-Alfaro, L. Lozano-Sánchez, S.-W. Lee, Rapid microwave-assisted synthesis of one-dimensional silver–H2Ti3O7 nanotubes, J. Mol. Catal. A Chem. 353 (2012) 163–170.

[73] C.E. Bamberger, G.M. Begun, Sodium titanates: stoichiometry and Raman spectra, J. Am. Ceram. Soc. 70 (3) (1987) (C-48-C-51).

[74] R. Ma, K. Fukuda, T. Sasaki, M. Osada, Y. Bando, Structural features of titanate nanotubes/nanobelts revealed by Raman, X-ray absorption fine structure and electron diffraction characterizations, J. Phys. Chem. B 109 (13) (2005) 6210–6214.

[75] T. Kasuga, M. Hiramatsu, A. Hoson, T. Sekino, K. Niihara, Titania nanotubes prepared by chemical processing, Adv. Mater. 11 (15) (1999) 1307.

[76] Z. Zhang, J.B. Goodall, S. Brown, L. Karlsson, R.J. Clark, J.L. Hutchison, I. Rehman, J.A. Darr, Continuous hydrothermal synthesis of extensive 2D sodium titanate (Na2Ti3O7) nano-sheets, Dalton Trans. 39 (3) (2010) 711–714.

[77] X.W. Huang, Z.J. Liu, Growth of titanium oxide or titanate nanostructured thin films on Ti substrates by anodic oxidation in alkali solutions, Surf. Coat. Tech. 232 (2013) 224–233.

[78] B. Zhao, L. Lin, D.N. He, Phase and morphological transitions of titania/titanate nanostructures from an acid to an alkali hydrothermal environment, J. Mater. Chem. A 1 (5) (2013) 1659–1668.

[79] R. Lu, J. Yuan, H.L. Shi, B. Li, W.Z. Wang, D.W. Wang, M.S. Cao, Morphology-controlled synthesis and growth mechanism of lead-free bismuth sodium titanate nanostructures via the hydrothermal route, Crystengcomm 15 (19) (2013) 3984–3991.

[80] Y. Mao, M. Kanungo, T. Hemraj-Benny, S.S. Wong, Synthesis and growth mechanism of titanate and titania one-dimensional nanostructures self-assembled into hollow micrometer-scale spherical aggregates, J. Phys. Chem. B 110 (2) (2006) 702–710.